Copy No. 11

DEFENCE R&D DÉFENSE

MICROSTRUCTURAL CHARACTERIZATION OF SAND CAST Ni-Al BRONZES

G. McMahon – J.A. Gianetto – M. Sahoo

MATERIALS TECHNOLOGY LABORATORY (CANMET)

DEFENCE RESEARCH ESTABLISHMENT ATLANTIC

Contractor Report

DREA CR 1999-042

April 1999

National Defence Défense nationale

Canada

102-02646/

National Defence
Research and Development Branch

Défense nationale
Bureau de recherche et développement

DREA CR 1999/042

Microstructural Characterization of Sand Cast Ni-Al Bronzes

G. McMahon – J.A. Gianetto – M. Sahoo

MATERIALS TECHNOLOGY LABORATORY (CANMET)
568 Booth street
Ottawa, ON, Canada
K1A 0G1

Scientific Authority C.V. Hyatt

April 1999

CONTRACTOR REPORT

Prepared for

Defence Research Establishment Atlantic

Centre de Recherches pour la Défense Atlantique

Canada

Materials Technology Laboratory

Microstructural Characterization of Sand-Cast Ni-Al Bronzes

G. McMahon, J.A. Gianetto and M. Sahoo

MTL 97-2(TR-R)

October 1997

CANMET

ABSTRACT

A study of the effect of alloy chemistry on the microstructure and microhardness of nickel aluminum bronze (NAB) with systematic changes in the Ni, Fe and Al content has been carried out for the reference alloy C95800. A further set of castings was made in order to investigate the effect of Cr, Ti and Zr additions, both singly and in combination, on the resultant microstructure and microhardness. All castings were characterized using optical microscopy and microhardness testing, and a select group was further characterized using scanning electron microscopy (SEM) and energy dispersive X-ray analysis (EDX). Most of these samples were also examined by secondary ion mass spectrometry (SIMS). The microstructures were found to be very sensitive to small changes in alloy chemistry.

RÉSUMÉ

Une étude de l'effet de la chimie des alliages sur la microstructure et la microdureté des bronzes au nickel-aluminium (NAB) en fonction des changements systématiques des teneurs en Ni, en Fe et en Al a été réalisée sur l'alliage de référence C95800. Une autre série de moulages a été faite pour étudier les effets de l'addition de Cr, de Ti et de Zr, seuls ou en mélange, sur la microstructure et la microdureté résultantes. Tous les coulages furent caractérisés par microscopie optique et un groupe choisi a aussi fait l'objet d'une caractérisation plus poussée par microscopie à balayage électronique (SEM) et par spectroscopie des rayons X par dispersion d'énergie (EDX). La plupart de ces échantillons furent aussi étudiés par spectrométrie de masse à émission ionique secondaire (SIMS). Les microstructures se sont révélées très sensibles à de petits changements de la chimie des alliages.

EXECUTIVE SUMMARY

The Defence Research Establishment Atlantic (DREA) has been conducting research and development work on laser surface melting and cladding of nickel aluminum bronze (NAB) alloys with the aim of developing surface modification techniques for restoration of valve components in sea water handling systems. Although NAB alloys generally have excellent corrosion, erosion and cavitation performance in sea water, and offer acceptable casting and fabrication characteristics, further research is required to ensure that optimal chemistries are developed and evaluated for these surface treatments.

A research project was initiated at MTL to systematically study the effect of alloy chemistry on the microstructure of NAB alloys based on the reference alloy C95800. Castings were made at MTL in the experimental casting laboratory with systematic changes in the Ni, Fe and Al content of the reference alloy. A further set of castings were made in order to investigate the effect of Cr, Ti and Zr additions, both singly and in combination, on the resultant microstructure and microhardness.

All castings were characterized using optical microscopy and microhardness testing, and a select group were further characterized using scanning electron microscopy (SEM) and energy dispersive X-ray analysis (EDX). A majority of these samples were also examined by secondary ion mass spectrometry (SIMS).

The results indicated that the microstructures were extremely sensitive to small changes in alloy chemistry. In particular, a change of less than one-half a percent of Al could have marked effect on the microstructure and microhardness of the material.

The effects of Ti and Cr on the microstructure seem to be fairly well understood, precipitating predominantly in the κ_I phase with Fe. However, Zr additions give rise to a new needle-like phase which requires further work to fully identify. The addition of all three modifying elements was found to have the effect of increasing the effective Al content.

CONTENTS

Page

EXECUTIVE SUMMARY ii

I. INTRODUCTION 1

2. EXPERIMENTAL METHODS 2

2.1 PRODUCTION OF EXPERIMENTAL CASTINGS 2

2.2 METALLOGRAPHY AND MICROHARDNESS TESTING 4

2.3 SCANNING ELECTRON MICROSCOPY (SEM) AND SECONDARY ION MASS SPECTROMETRY (SIMS) 4

3. RESULTS 4

3 1 CHEMICAL COMPOSITIONS OF NAB CASTINGS 4

3.2 MICROSTRUCTURE AND HARDNESS - SERIES A1 5

3.3 MICROSTRUCTURE AND HARDNESS - SERIES A2 7

3.4 MICROSTRUCTURE AND HARDNESS - SERIES B1 8

3.5 MICROSTRUCTURE AND HARDNESS - SERIES B2 9

3.6 MICROSTRUCTURE AND HARDNESS - SERIES B3 10

3.7 MICROSTRUCTURE AND HARDNESS - SERIES B4 11

3.8 MICROSTRUCTURE AND HARDNESS - SERIES C1 12

3.9 MICROSTRUCTURE AND HARDNESS - SERIES C2 13

3.10 MICROSTRUCTURE AND HARDNESS - SERIES C3 14

3.11 MICROSTRUCTURE AND HARDNESS - SERIES D1 15

3.12 SEM & EDS 16

3.12.1 Sample 124-95-1 (Series A1, 9.3% Al, 4.6% Ni, 4.8% Fe) 17

3.12.2 Sample 124-95-3 (Series A1, 12.5% Al, 4.6% Ni, 4.6% Fe) 17

3.12.3 Sample 136-95-2 (Series A2, 9.3% Al, 4.6% Ni, 6.1% Fe) 18

3.12.4 Sample 140-95-3 (Series D1, 7.8% Al, 3.7% Ni, 4.4% Fe, 1.12% Cr, 0.79% Ti, 0.68% Zr) 18

4. DISCUSSION 20

5. CONCLUSIONS 23

6. RECOMMENDATIONS FOR FUTURE WORK 24

7. ACKNOWLEDGMENTS 25

8. REFERENCES 26

I. INTRODUCTION

The Defence Research Establishment Atlantic (DREA) has been conducting research and development work on laser surface melting and cladding of nickel aluminum bronze (NAB) alloys with the aim of developing surface modification techniques for restoration of valve components in sea water handling systems (1,2). Although NAB alloys generally have excellent corrosion, erosion and cavitation performance in sea water, and offer acceptable casting and fabrication characteristics, further research is required to ensure that optimal chemistries are developed and evaluated for these surface treatments.

The NAB alloy (C95800) generally used in marine applications has a nominal composition of 9.0 wt % Al, 4.5 wt % Ni, 4.0 wt % Fe, 1.2 wt % Mn and the balance Cu. The binary copper-aluminum alloy has no commercial applications, but knowledge of its equilibrium microstructure aids in the interpretation of the microstructures of the more complex alloys encountered in the present work. For binary alloys containing more than 9.4 wt % Al, an $\alpha + \beta$ structure is obtained at temperatures above 565°C as evident from the phase diagram shown in Fig. 1. Decomposition of the β phase will occur during cooling or annealing below 565°C to form the $\alpha + \gamma_2$ eutectoid. The formation of this eutectoid decreases both the mechanical properties and corrosion resistance, and therefore, various methods have been developed to reduce or eliminate the γ_2 phase. It has been suggested that, by annealing the alloy between 600-800°C and quenching rapidly, the diffusional β transformation can be suppressed. If the cooling rate is insufficient, the γ_2 phase may still be formed (3). A second idea was to add alloying elements which would inhibit the formation of γ_2 without having deleterious effects on the mechanical properties (3). The alloying elements used for this purpose are Fe, Ni and Mn, which represent the NAB alloy now used in most applications.

A phase diagram from the system with 5% Ni and 5% Fe is shown in Fig. 2 (4). The Ni and Fe used in this alloy combine with Al to form one of four different intermetallic phases collectively known as the κ phase, and differentiated by the subscripts I, II, III and IV. Initially, these phases were classified on the basis of morphology (5), however, information pertaining to the chemistry of these phases based on electron beam microanalysis is now available, (3,6,7). The final microstructure produced under normal casting conditions can be described as a Cu-rich solid solution α phase, various κ phases and some retained β phase. A schematic diagram indicating the different phases observed is illustrated in Fig. 3 (6), and approximate chemical compositions of each phase are given in Table 1.

The present work was designed to allow a systematic study of the influence of alloy composition on (a) sand-cast structure and microhardness and (b) response to a wide range of laser melting conditions. Formation of the complex intermetallic compounds formed in the

traditional NAB alloys described above were further altered by additions of Cr, Ti and Zr, both singly and in combination. This report summarizes their influence on the as-cast microstructure and hardness, while the effect of laser melting experiments are being evaluated at DREA. Future studies will focus on transformation behaviour using dilatometry, Gleeble simulation of weld metal and heat-affected zone regions, and on corrosion behaviour.

Table 1. Compositions of the various phases in NAB from the Cu-Al-Fe-Ni system.

Phase	Cu	Al	Fe	Ni	Mn	Si	Ref
κ_I	15 ± 5	13 ± 5	55 ± 7	15 ± 3	2 ± 0.4		3
	10.5±1.0	9.3 ± 0.5	72.2 ± 1.4	3.5 ± 0.4	2.9 ± 0.5	1.6 ± 0.4	6
κ_{II}	23±4	18±4	34 ± 5	24 ± 5	1.6±0.3	--	3
	26.9	26.0	24.1	21.3	1.7	--	8
	12.1 ± 3.1	12.3 ± 1.3	61.3 ± 4.9	8.0 ± 1.8	2.2 ± 0.2	4.1 ± 0.8	6
κ_{III}	26 ± 4	22 ± 4		28 ± 5	1.6 ± 0.4	--	3
	30.6	28.3	18.5	20.7	1.9	--	8
	17.0 ± 4.6	26.7 ± 1.0	12.8 ± 1.6	41.3 ± 6.0	2.0 ± 0.4	<0.1	6
κ_{IV}	23 ± 6	9 ± 4	60 ± 8	6 ± 4	1.6 ± 0.4	--	3
	30	13	51	4	2	--	8
	2.6 ± 0.7	10.5 ± 1.7	73.4 ± 2.3	7.3 ± 1.5	2.4 ± 0.2	4.0 ± 0.5	6
β	85.2	8.7	1.6	3.5	1.0	--	3

2. EXPERIMENTAL METHODS

2.1 PRODUCTION OF EXPERIMENTAL CASTINGS

In total, 30 NAB alloys were prepared in the MTL experimental casting laboratory by induction melting in a 100 kW and 3000 Hz push-up furnace using a clay-graphite crucible and casting into green sand moulds to produce plates (305 x 152 x 25 mm). The alloys were based on the reference composition of C95800 shown in Table 2.

For the present investigation, the major alloying elements Al, Ni and Fe, as well as additions of Cr, Ti and Zr were varied systematically to generate ten series of experimental alloys. This allowed various effects to be studied independently, including not only the effect of the Cr, Ti and Zr additions, but also the effect of changing the Ni/Fe ratio at four different Al concentrations, as well as changing the Al content at two different but constant Ni/Fe ratios. The experimental design is described in Table 3

Table 2. Reference composition of alloy C95800 and targeted base composition for the experimental alloys.

Specification	Al (wt %)	Ni (wt %)	Fe (wt %)	Mn (wt %)	Cu
Range	8.5-9.5	4.0-5.0	3.5-4.5	0.8-1.5	balance
Targeted	9.5	5.0	5.0	1.0	balance

Three casting compositions were produced from each 90 kg heat by melting the major alloying elements (ETP Cu, Cu-30% Ni, Cu-10% Fe and electrolytic Mn) and adjusting the composition before and after each pour. The temperature of the melt was increased to between 1180 and 1220°C and degassed with dry nitrogen for 10 min. Once the first set of two plates was poured, the crucible was returned to the furnace, and further adjustments were made to the chemistry. This process was repeated for the second and third sets of plates. The final chemical composition of the alloys was determined by optical emission spectroscopy.

Table 3. Experimental design to study effect of alloying elements on microstructure and hardness.

Series	Effect to be studied
A1	Increase in Al with constant Ni/Fe ratio of ~1.0
A2	Increase in Al with constant Ni/Fe ratio of ~0.74
B1	Change of Ni/Fe ratio at ~9.1 wt % Al
B2	Change of Ni/Fe ratio at ~10.1 wt % Al
B3	Change of Ni/Fe ratio at ~11.3 wt % Al
B4	Change of Ni/Fe ratio at ~12.2 wt % Al
C1	Effect of Cr addition
C2	Effect of Ti addition
C3	Effect of Zr addition
D1	Effect of Cr, Ti and Zr addition

Since aluminum bronzes are dross-forming alloys, pressed ceramic filters (Flow-Rite) were used in the gating system to minimize the entrapment of dross inclusions. Electrolytic Cr and sponge Ti and Zr were added to modify the as-cast microstructure as described in Table 3. Of all these alloys, only Zr additions in excess of 1% caused problems in mould filling. In this case, the pouring temperature of 1180°C was considered to be too low, and the formation of an

oxide film during pouring produced cold shuts and laps in the plate castings. As a result, these castings were discarded

2.2 METALLOGRAPHY AND MICROHARDNESS TESTING

A full-thickness sample from each experimental alloy was sectioned, mounted and prepared using standard metallographic techniques. The final polishing was completed using a vibratory polisher with a solution of ethylene glycol and magnesium oxide (0.05 μm). Each sample was etched in an alcoholic ferric chloride solution.

The microhardness testing was performed using a diamond pyramid indenter with a 100 g load to facilitate measurements of specific microstructural constituents.

2.3 SCANNING ELECTRON MICROSCOPY (SEM) AND SECONDARY ION MASS SPECTROMETRY (SIMS)

To assist with the interpretation of the complex microstructures and in particular to characterize the various κ phases, selected specimens were chosen for further detailed analysis using SEM and SIMS.

A Philips XL30 SEM was used to obtain both secondary and backscattered electron images. Energy-dispersive X-ray analysis (EDX) was also used to obtain chemical compositions of selected phases in the microstructure.

The low concentrations (<1 wt %) of the Cr, Ti and Zr alloy additions led us to believe that SIMS analyses would be useful to identify qualitatively the chemical constituents of the individual phases. With detection limits extending to the ppb range, detection of these alloying elements would present no difficulty for SIMS. Furthermore, the rapid acquisition (100 s or less) of element-specific ion images led to the use of SIMS for most of the alloys studied. Analyses were performed using a Cameca IMS 4f magnetic sector dynamic SIMS. An O_2^+ primary ion beam was used, and positive secondary ions were detected. This experimental procedure enhances the secondary ion yield of all elements of interest in this study. Digital direct ion images were acquired using a resistive anode encoder (RAE) following a pre-sputter of the surface to remove any oxide films or residue left from the etchant. The appropriate mass resolving aperture was selected to ensure that no mass interferences contributed to the ion image.

3. RESULTS

3.1 CHEMICAL COMPOSITIONS OF NAB CASTINGS

The chemical compositions of the NAB alloys are given in Table 4. As indicated, the series A1 and A2 alloys had increasing Al contents with two different but constant Ni:Fe ratios In series B, there was, in general, good control of chemical compositions with variations in the

Ni:Fe ratios with constant Al levels being achieved. For the C series alloys, there was reasonably good control of the compositions in melt #137, where the Cr content was increased from 0.61 to 1.72 wt %. In melt #103, with Ti content increasing from 1.08 to 3.55 wt %, a slightly higher Fe concentration and lower Mn content resulted. For melt #114, the only sound casting produced was obtained with the lowest (0.97 wt %) Zr content, as explained earlier. Although increasing levels of Cr, Ti and Zr were achieved in the D series alloys, this was accompanied by simultaneous decreases in Al, Ni and Fe, as shown in Table 4.

3.2 MICROSTRUCTURE AND HARDNESS - SERIES A1

In series A1, the effect of increasing the Al content from 9.3 to 12.5 wt % at a Ni:Fe ratio of approximately 1.0 and average Ni and Fe concentrations of 4.7 wt % was investigated. The typical microstructure for the alloys with the lowest Al concentration is shown in Fig. 4. At low magnification [Fig. 4(a)], both columnar and equiaxed α grains are evident. All the phases represented in Fig. 3 except κ_I are observed [Figs. 4(b) and (c)].

The dark-etching particles in the proximity of the α grain boundaries are κ_{II} particles, and are approximately 2 μm in diameter. The lamellar phase observed at many of the α grain boundaries is the typical morphology of the κ_{III} phase. In some cases this phase may be observed in cross-section and resemble the κ_{II} phase, so care should be taken to distinguish between the two. At higher magnification [Fig. 4(b)], small κ_{IV} particles less than 1 μm in size are observed within the α grains. There also appears to be a κ_{IV} precipitate-free zone extending 1-2 μm from the α grain boundaries. Finally, some dark-etching retained β phase surrounded by the κ_{III} phase can be seen in Fig. 4(c). However, there was no evidence of the prior β grain boundaries.

SIMS direct ion images for Fe, Ni and Cu are shown in Fig. 5. The κ_{IV} particles are below the spatial resolution of the technique (1 μm), however, the Fe-enriched κ_{II} particles 2-3 μm in size are readily observed in Fig. 5(a). A low Cu content of these particles compared to the α matrix is indicated in Fig. 5(c). The areas of slight Ni enrichment seen in Fig. 5(b) result from the high density of the κ_{III} phase at the α grain boundaries. Although both dimensions of the phase are below the spatial resolution of the technique, its high area fraction in those specific regions results in the enriched areas shown in the SIMS image.

As the concentration of Al is raised to 10.7 wt %, marked changes are observed in the microstructure, indicated by the micrographs shown in Fig. 6. At low magnification, as in Fig. 6(a), the prior β boundaries become clearly visible. The α grains form a lath-like structure and, at a higher magnification, as in Fig. 6(b), a uniform distribution of the κ_{II} particles is observed throughout the sample. The κ_{IV} phase continues to be present within the α grains, and it is evident that less κ_{III} has formed. A clear difference, however, is an increase in the proportion of retained β phase.

Table 4. Final composition (in wt %) of experimental alloys used in this study.

Series	Melt No.	Al	Ni	Fe	Mn	Ni/Fe	Cr	Ti	Zr
A1	124-95-1	9.3	4.6	4.8	1.1	0.96	--	--	--
	124-95-2	10.7	4.7	4.7	1.1	1.00	--	--	--
	124-95-3	12.5	4.6	4.6	1.0	1.00	--	--	--
A2	136-95-1	8.8	4.6	6.2	1.1	0.74	--	--	--
	136-95-2	9.3	4.6	6.1	1.1	0.74	--	--	--
	136-95-3	9.7	4.6	6.2	1.1	0.74	--	--	--
B1	128-95-1	9.1	5.0	4.7	1.1	1.05	--	--	--
	128-95-2	9.2	6.5	4.6	1.1	1.41	--	--	--
	128-95-3	9.2	6.5	5.7	1.0	1.14	--	--	--
B2	125-95-1	10.1	3.8	3.9	1.0	0.97	--	--	--
	125-95-3	10.1	3.8	5.5	1.0	0.69	--	--	--
B3	132-95-1	11.3	4.1	4.3	1.0	0.95	--	--	--
	132-95-2	11.3	4.1	5.0	1.0	0.82	--	--	--
	132-95-3	11.3	4.0	5.8	0.95	0.69	--	--	--
B4	133-95-1	12.2	4.7	3.8	1.3	1.24	--	--	--
	133-95-2	12.2	5.9	4.2	1.3	1.40	--	--	--
	133-95-3	12.2	6.1	6.5	1.2	0.93	--	--	--
C1	137-95-1	9.6	5.2	4.8	1.1	1.08	0.61	--	--
	137-95-2	9.8	5.2	5.6	1.1	0.92	1.15	--	--
	137-95-3	9.6	5.1	6.3	1.1	0.81	1.72	--	--
C2	103-95-1	10.0	5.0	6.3	0.31	0.80	--	1.08	--
	103-95-2	9.7	5.1	6.2	0.35	0.82	--	2.24	--
	103-95-3	9.6	5.0	6.1	0.36	0.82	--	3.55	--
C3	114-95-1	9.4	5.0	6.0	0.83	0.83	--	--	0.97
D1	140-95-1	9.3	4.9	5.3	1.1	0.92	0.31	0.23	0.23
	140-95-2	8.9	4.7	5.0	1.0	0.94	0.60	0.44	0.41
	140-95-3	7.8	3.7	4.4	0.91	0.84	1.12	0.79	0.68

A high Al content of 12.5 wt % produces well-defined prior β boundaries as evidenced by Fig. 7(a). The lath-like structure of the α phase is much finer, and takes on the appearance of a bainitic or Widmanstatten morphology. A large number of κ_{II} particles are observed throughout the sample, with a striking feature being their decoration of the prior β boundaries, as observed in Fig. 7(b) and (c).

Ion images for Fe and Ni are shown in Fig. 8, where a strong enrichment of Fe in the κ_{II} particles can be observed. A slight Ni enrichment is also evident. An interesting feature is the strong Ni enrichment observed at the boundary, as shown in Fig. 8(b). Such an enrichment is more typical of the κ_{III} phase, however, the lamellar structure associated with this phase was not observed.

The average microhardness values and range of data for this series of alloys are given in Table 5. A slight increase in hardness is observed with an increase in Al concentration from 9.3 to 10.7 wt %. A more dramatic increase results upon a further increase to 12.5 wt % Al.

Table 5. Microhardness data from alloy series A1 samples.

Series	Melt No.	Al	Ni/Fe	Avg hardness	
				VHN	Range
A1	124-95-1	9.3	0.96	172	159-201
	124-95-2	10.7	1.00	218	195-247
	124-95-3	12.5	1.00	307	284-340

3.3 MICROSTRUCTURE AND HARDNESS - SERIES A2

The microstructure for an alloy with excess Fe (Ni:Fe ratio of 0.74) and 8.8 wt % Al is shown in Fig. 9. Equiaxed α grains are observed at a low magnification in Fig. 9(a), while in Fig. 9(b) at a higher magnification, all four κ phases can be identified. The large rosette-shaped phase is typical for κ_I, while globular κ_{II} phases can be seen in the proximity of the α grain boundaries. Lamellar κ_{III} is also observed, while numerous κ_{IV} particles are present within the α grains.

The effect of increasing the Al content to 9.3 wt % on the microstructure is given by the micrographs of Fig. 10. This alloy can be directly compared with alloy 124-95-1 to show the effect of the decrease in the Ni:Fe ratio, as both samples have identical Al compositions. In this case. the α grains take on a slightly more columnar appearance with a relatively finer grain size, and all four κ phases are again present. There is little difference in the microstructure between this sample and that with 8.8 wt % Al, with the exception of the decrease in the α grain size with the higher Al content.

Ion images for Fe, Ni and Cu are shown in Fig. 11, where the Fe enrichment of the κ_I and κ_{II} phases becomes apparent. Variations in the Fe and Cu concentrations within the κ_I phase are also notable.

A further increase in the Al content to 9.7 wt % leads to an α grain structure which is more columnar in nature, as evidence by Fig. 12(a). All four κ phases can again be observed in Fig. 12(b) and (c), as well as a notable fraction of the retained β phase.

The average microhardness and range of values for this series of alloys are given in Table 6. As might be expected from the similarities of the microstructures, little change is observed in the microhardness values with increasing Al content.

Table 6. Microhardness data from Alloy series A2 samples.

Series	Melt No.	Al	Ni/Fe	Avg hardness	
				VHN	Range
A2	136-95-1	8.8	0.74	175	136-226
	136-95-2	9.3	0.74	185	159-220
	136-95-3	9.7	0.74	178	163-211

3.4 MICROSTRUCTURE AND HARDNESS - SERIES B1

In the B series of alloys, the effect of altering the Ni:Fe ratio at various Al levels was investigated. The lowest Al level used was 9.2 wt % for the B1 series. Micrographs from the alloy with a Ni:Fe ratio of 1.06 are shown in Fig. 13. The structure consists of columnar and equiaxed α grains, and at higher magnifications, all phases except κ_I are evident in Fig. 13(b) and (c). These micrographs are similar to those shown in Fig. 4(b) and (c) except that a relatively higher volume fraction of κ_{III} is present probably because of the higher nickel content. As with sample 124-95-1, a κ_{IV} precipitate free zone extending 1-2 μm from the α grain boundaries is noted.

SIMS direct ion images for Fe and Ni are shown in Fig. 14. The Fe-enriched κ_{II} phase is discernible in the Fe image, while the Ni image shows the Ni-enriched lamellar κ_{III} phase rather well. There also appears to be a slight Fe enrichment within the κ_{III} phase, as would be expected from the reported composition of this phase.

Increasing the Ni:Fe ratio to 1.41 produces the microstructures shown in Fig. 15. Little change is observed in the α grain structure, with perhaps the only difference being a slightly stronger tendency towards a columnar morphology. At higher magnifications, however, significant differences can be elucidated. The fraction of the lamellar κ_{III} phase has increased dramatically, apparently at the expense of the κ_{II} phase which is no longer visible. The κ_{IV} phase retains its location within the α grains, but as with the previous sample, a κ_{IV} precipitate free zone extending 1-2 μm from the α grain boundaries is observed.

SIMS images for Fe and Ni shown in Fig. 16 confirm the high density of the κ_{III} phase. Many Ni-enriched lamellar phases are observed. However, the Fe image shows that this phase is slightly more enriched in Fe than the previous sample.

The effect of changing the Ni:Fe ratio back down to 1.14 by leaving the Ni at a relatively high level of 6.5 wt % and raising the Fe concentration to 5.7 wt % is shown by the micrographs in Fig. 17. The α grains are observed to form with a columnar morphology, while at higher magnification, a return of the κ_{II} phase at the expense of some κ_{III} phase is evident. The location of the κ_{IV} phase remains within the α grain interior, with the κ_{IV} precipitate free zone again notable.

Direct ion images for Fe and Ni are given in Fig. 18 and are in good agreement with the previous images for this alloy series, with the images showing Ni and Fe enriched κ_{III} phases. Images from a second region showing a high density of κ_{II} particles are also shown in this figure, which indicate that substantial Ni enrichment is observed in the κ_{II} phase.

The average microhardness and range of values for this sample are given in Table 7. Little change in the microhardness is observed with alterations of the Ni:Fe ratio, not an unexpected result given the similarities in the microstructures.

Table 7. Microhardness data from alloy series B1 samples.

Series	Melt No.	Al	Ni/Fe	Avg hardness	
				VHN	Range
B1	128-95-1	9.1	1.06	187	169-199
	128-95-2	9.2	1.41	190	177-201
	128-95-3	9.2	1.14	202	179-224

3.5 MICROSTRUCTURE AND HARDNESS - SERIES B2

The effect of increasing the Al content to 10.1 wt % and changing the Ni:Fe ratio was investigated in this set of alloys. For a Ni:Fe ratio of 0.97, and relatively low Ni and Fe contents (3.8 and 3.9 wt %, respectively), the resulting microstructures are shown in Fig. 19. Columnar and, to some extent, acicular α grains are noted, with κ_{IV} particles being located within their interior. The κ_{II} phase can be observed near the α grain boundaries, while a small fraction of the lamellar κ_{III} phase is observable. A significant portion of retained β is also evident, and the prior β boundaries appear to be delineated by the α grains.

Decreasing the Ni:Fe ratio to 0.69 by raising the Fe content to 5.5 wt % leads to the microstructures shown in Fig. 20. A less acicular and more columnar-like appearance of the α

grains is noted. At a higher magnification, as in Fig. 20(b), the κ_{IV} particles can be seen within the α grain interiors. The κ_{II} phase is now observed to be located not only in the vicinity of the grain boundaries, but also within the α grains where they take on more of a rosette-like morphology with a maximum dimension of roughly 15 μm, slightly smaller than would be expected for the κ_I phase which takes on a similar morphology. Nevertheless, a κ_I rosette 20-30 μm in size is also observed in Fig 20(b). A significant portion of retained β is again evident, although no evidence of prior β boundaries is present.

The microhardness data for this set of samples is given in Table 8, which again shows little difference in the average microhardness, reflecting the similarities of the microstructures.

Table 8. Microhardness data from alloy series B2 samples.

Series	Melt No.	Al	Ni/Fe	Avg hardness	
				VHN	Range
B2	125-95-1	10.1	0.97	195	166-222
	125-95-3	10.1	0.69	181	160-228

3.6 MICROSTRUCTURE AND HARDNESS - SERIES B3

For the series B3 alloys, the Al content was further raised to 11.3 wt %. and the effect of changing the Ni:Fe ratio at a constant Ni concentration of 4.1 wt % was studied. The resultant microstructures for the alloy with a Ni:Fe ratio of 0.95 are shown in Fig. 21. The prior β boundaries are clearly visible and delineated by α grains, and a high fraction of retained β is present. The α grains are seen to be quite acicular and form a lath-like structure. At a higher magnification, many κ_{II} particles distributed uniformly throughout the sample can be observed, while only small amounts of the κ_{III} and κ_{IV} phases are discernible, only within the acicular α grains.

Decreasing the Ni:Fe ratio to 0.82 by increasing the Fe content to 5.0 wt % has the main effect of coarsening the α grains such that they are less acicular in nature. This is evident in the micrographs of Fig. 22, which also show comparable fractions of retained β and κ_{II} particles. Only small amounts of κ_{III} phase are observed, and it may be argued that more κ_{IV} particles within the α grains have formed.

A final decrease of the Ni:Fe ratio to 0.69 by increasing the Fe content to 5.8 wt % led to the microstructures shown in Fig. 23. A decrease in the size of the prior β grains delineated by the α grains is evident. A further coarsening of the α grains has also resulted from the decrease in the Ni:Fe ratio. At a higher magnification, an increase in the size of the κ_{II} particles to about

8-10 μm accompanied by a tendency to acquire a more rosette-like morphology has occurred. A significant portion of retained β is present, and the presence of the κ_{III} and κ_{IV} phases remains small.

With decreasing Ni:Fe ratios, there was a slight decrease in average microhardness (Table 9) which resulted from both the coarsening of the α grains and the increase in the size of the κ_{II} particles.

Table 9. Microhardness data from alloy series B3 samples

Series	Melt No.	Al	Ni/Fe	Avg hardness	
				VHN	Range
B3	132-95-1	11.3	0.95	272	243-308
	132-95-2	11.3	0.82	250	227-275
	132-95-3	11.3	0.69	245	205-322

3.7 MICROSTRUCTURE AND HARDNESS - SERIES B4

The effect of a final increase in the Al content to a value of 12.2 wt % and varying Ni:Fe ratios and varying Ni and Fe contents was investigated in series B4.

The micrographs in Fig. 24 show the microstructure of the alloy with 4.7 wt % Ni and 3.8 wt % Fe, yielding a Ni:Fe ratio of 1.24. The prior β boundaries are evident, and a very fine lath-like structure of the α phase, similar to a bainitic or Widmanstatten structure, is observed. A high density of κ_{II} particles is visible throughout the structure.

Increasing the Ni:Fe ratio to 1.40 with a simultaneous increase in the Ni and Fe concentrations to 5.9 and 4.2 wt %, respectively, leads to the microstructures shown in Fig. 25. Again, the prior β boundaries delineated by α grains and a high fraction of retained β are observed. A slight coarsening of the α grains has resulted, and again κ_{II} particles are present throughout the sample.

The effect of a decrease in the Ni:Fe ratio to 0.93 resulting from an increase in the Ni and Fe concentrations to 6.1 wt % and 6.5 wt %, respectively, on the microstructure is represented by the micrographs shown in Fig. 26. The prior β boundaries and retained β phase remain clearly visible, although in this case the prior β grains appear to have been smaller. The changes in the alloy composition appear to have had little effect on the morphology of the α grains.

The coarsening of the α grain structure away from the initial bainitic or Widmanstatten morphology with changes in the alloy chemistry is reflected in the microhardness data given in Table 10. A high value is observed for the initial sample in the series, while the latter two samples show similar but lower values, a result of their coarser α grain structure.

Table 10. Microhardness data from alloy series B4 samples.

Series	Melt No.	Al	Ni/Fe	Avg hardness	
				VHN	Range
B4	133-95-1	12.2	1.24	304	287-330
	133-95-2	12.2	1.40	274	265-281
	133-95-3	12.2	0.93	276	250-291

3.8 MICROSTRUCTURE AND HARDNESS - SERIES C1

The effect of increasing Cr additions and decreasing Ni:Fe ratios at a constant Al content of roughly 9.7 wt % was investigated by the C1 series of alloys. The micrographs in Fig. 27 show the result of a 0.61 wt % Cr addition to an alloy with a Ni:Fe ratio of 1.08 on the microstructure. The α grains are of columnar morphology, and many small patches of the retained β phase are observed. At higher magnification, κ_{IV} particles can be observed within the α grains, and an abundance of the lamellar κ_{III} phase is also clear. A smaller amount of the κ_{II} phase is present.

Increasing the Cr content to 1.15 wt % and the Fe concentration to 5.6 wt % to give a Ni:Fe ratio of 0.92 yields the microstructures shown in Fig. 28. The morphology of the α grains remains about the same, however, an increase in the fraction of the retained β phase is apparent. At higher magnifications, an increase in the amount of the κ_I phase, seemingly at the expense of the κ_{III} phase, has occurred. Some smaller κ_{II} particles remain visible.

SIMS direct ion images for this sample are quite revealing. The images for Fe, Ni, Cu and Cr are shown in Fig. 29. The Fe enrichment of the κ_I phase observed in the Fe ion image is striking, and by comparing this image to those of the other elements, a strong enrichment of Cr is also observed, while a depletion of Ni and Cu is evident. Similarly, smaller κ_{II} particles are also observed to be Fe and Cr enriched. Enrichment of Ni in the κ_{III} phase can be deduced through examination of the Ni ion image. A slight increase in Fe is also observed in these areas.

A further increase in the Cr concentration to 1.72 wt % accompanied by an increase in the Fe content to 6.3 wt %, giving a Ni:Fe ratio of 0.81, produced the microstructures shown in Fig. 30. Little change is again observed in the α grain size and morphology. The size and quantity of the κ_I phase has increased dramatically, with the rosettes taking on a more dendritic morphology, and dimensions extending to 100 μm along the primary dendrite arms. Extensive regions of lamellar κ_{III} phase remain, while only a small amount of κ_{II} particles are observed. Small κ_{IV} particles are again evident within the α grain interiors.

The average microhardness and range of values for this series of alloys are given in Table 11, and little difference is observed between the three alloys. The similarity in the microstructures of the three alloys reflect these results.

Table 11. Microhardness data from alloy series C1 samples.

Series	Melt No.	Al	Ni/Fe	Cr	Ti	Zr	Avg hardness	
							VHN	Range
C1	137-95-1	9.6	1.08	0.61	--	--	185	158-204
	137-95-2	9.8	0.92	1.15	--	--	202	167-267
	137-95-3	9.6	0.81	1.72	--	--	204	158-264

3.9 MICROSTRUCTURE AND HARDNESS - SERIES C2

The effect of increasing Ti additions on alloys with slight reductions in Al contents and constant Ni:Fe ratios was examined in the C2 alloy series. For an Al concentration of 10.0 wt %, a Ti addition of 1.08 wt % and a Ni:Fe ratio of 0.80, the resulting microstructures are shown in Fig. 31. The first feature to be noted is that the α grains have now taken an equiaxed structure. Many small patches of dark-etching retained β are also observed. Numerous κ_I rosettes are seen throughout the microstructure. The smaller κ_{II} particles are once again observed in the proximity of the α grain boundaries, while the κ_{IV} particles retain their usual location within the α grains. Very little of the κ_{III} phase is present.

SIMS direct ion images for Cu, Fe, Ni and Ti are reproduced in Fig. 32 and show some surprising results. The Fe enrichment of the roughly 20 μm-sized κ_I rosettes does not come unexpected, however these rosettes are also rich in Ti, and surprisingly in Ni. A smaller enrichment of Ni is observed in the smaller Fe-rich κ_{II} particles, which also show a slight enrichment in Ti.

The effect of increasing the Ti content to 2.24 wt %, while simultaneously lowering the Al content to 9.7 wt % and keeping the Ni:Fe ratio constant at a value of 0.82 on the resulting microstructures is shown in Fig. 33. The equiaxed nature of the α grains is again evident, and the dispersion of the κ_I rosettes, now increased in size to approximately 60 μm, is striking. At higher magnifications, the microstructure is dominated by the κ_I phase. The smaller κ_{II} particles remain in the vicinity of the α grain boundaries, while the κ_{IV} phase is still observable within the α grains. Very little, if any, κ_{III} phase is present.

A final increase in the Ti content to 3.55 wt % with roughly the same Al concentration (9.5 wt %) and Ni:Fe ratio led to the microstructures shown in Fig. 34. The same general trend is observed, whereby the α grains remain equiaxed, the κ_I phase continues to dominate the

microstructure and had increased in size again to roughly 75 μm. Otherwise, only the κ_{II} and κ_{IV} phases are observable, in their usual locations.

The microhardness data for this series of alloys is given in Table 12, and although little difference is observed in the average value, a relatively large spread in the data is clear, particularly for the latter two alloys. This may be a result of the inhomogeneity of the microstructure because of their larger κ_I rosettes.

Table 12. Microhardness data from alloy series C2 samples.

Series	Melt No.	Al	Ni/Fe	Cr	Ti	Zr	Avg hardness	
							VHN	Range
C2	103-95-1	10.0	0.80	--	1.08	--	206	183-243
	103-95-2	9.7	0.82	--	2.24	--	217	155-317
	103-95-3	9.6	0.82	--	3.55	--	217	136-291

3.10 MICROSTRUCTURE AND HARDNESS - SERIES C3

As mentioned earlier, problems were encountered for the alloys with Zr additions of greater than 1 wt %, as the formation of oxide films during pouring produced cold shuts and laps within the castings. As a result, only one casting in series C3 was sound, containing 0.97 wt % Zr with an Al content of 9.4 wt % and a Ni:Fe ratio of 0.83.

The microstructures for this alloy are shown in Fig. 35 and are characterized by equiaxed α grains. The κ_I phase takes on both a rosette and possibly a thin needle-like morphology. Many κ_{II} particles are observed in the proximity of the α grain boundaries, and a high density of κ_{IV} particles are observed within the α grains. Very little κ_{III} phase is present.

SIMS direct ion images for Fe, Ni, Cu and Zr are shown in Fig. 36. A fairly large rosette is found to be enriched in Fe, as would be expected. Some Ni is also seen to be present in this phase, while a non-uniform distribution of Cu is evident. In contrast to Cr and Ti, which tended to concentrate with the κ_I phase, little Zr is observed within the rosette. Rather, the needle-like and globular phases noted in the micrographs appear to be very rich in Zr. Some κ_{II} particles showing enrichments in Fe and, to a lesser extent, Ni are also visible.

The microhardness data for this material is given in Table 13 and indicates a much narrower spread in the data than for the alloys in series C2.

Table 13. Microhardness data from alloy series C3 sample.

Series	Melt No.	Al	Ni/Fe	Cr	Ti	Zr	Avg hardness	
							VHN	Range
C3	114-95-1	9.4	0.83	--	--	0.97	185	165-205

3.11 MICROSTRUCTURE AND HARDNESS - SERIES D1

The effect of adding all three of the modifying elements Cr, Ti and Zr in increasing total amounts with decreasing Al content was investigated in this series. For an Al content of 9.3 wt % and Cr, Ti and Zr levels of 0.31, 0.23 and 0.23 wt %, respectively, the microstructures produced are shown in Fig. 37. The α grains are seen to be equiaxed in nature, and a significant fraction of retained β can be observed. Some κ_{II} and κ_{IV} particles are also discernible. Only a small fraction of the κ_{III} phase is present. A needle-like phase similar to that found in the series C3 alloy, is also noticeable.

A further increase in the Cr, Ti and Zr levels to 0.60, 0.44 and 0.41 wt %, respectively, and a decrease in the Al content to 8.9 wt % produces the microstructures shown in Fig. 38. All phases are readily identifiable in the microstructure: κ_I rosettes 20 μm in size, κ_{II} particles at, and in the vicinity of the α grain boundaries, κ_{IV} particles within the equiaxed α grains, the lamellar κ_{III} phase, and the needle-like Zr-rich phase. Some retained β phase is also present, the area fraction being somewhat less than with the previous alloy.

A final increase of the Cr, Ti, and Zr levels to 1.12, 0.79 and 0.68 wt % with a simultaneous decrease in the Al content to 7.8 wt % produces the microstructures shown in Fig. 39. The κ_I rosettes and Zr-rich needles are seen, while the κ_{IV} particles within the α grains appear to have coarsened. Some κ_{II} particles remain visible, but the most notable difference is the phase present along the α grain boundaries which, on the basis of these micrographs alone, is not easily classifiable. A further decrease in the amount of the retained β phase is also evident.

SIMS direct ion images for Al, Ti, Fe, Cr, Ni, Cu and Zr are shown in Fig. 40, encompassing an area showing both the unknown boundary phase and the needle-like phase. The boundary phase, observed near the bottom of the ion images, appears to be enriched in Ti, Cr, Zr and Fe, and shows a depletion of Ni, Cu and Al.

Further ion images showing κ_I rosettes are given in Fig. 41 and are found to be enriched in Fe and Cr, with smaller enrichments in Ti. A depletion of Cu is also observed. On the other hand, the smaller κ_{II} particles show strong enrichments in Fe, Ti and Ni, with weaker enrichments in Cr and Zr, and again a depletion of Cu.

Table 14. Microhardness data from alloy series D1 samples.

Series	Melt No.	Al	Ni/Fe	Cr	Ti	Zr	Avg hardness	
							VHN	Range
D1	140-95-1	8.8	0.92	0.31	1.08	0.23	179	161-203
	140-95-2	9.3	0.94	0.60	2.24	0.41	179	161-197
	140-95-3	9.7	0.84	1.12	3.55	0.68	187	149-247

The microhardness data for this series of samples reflects their similar microstructures in that relatively little change is noted in the average microhardness. The data are summarized in Table 14.

3.12 SEM & EDS

Selected samples were examined in the SEM and numerous phases were analyzed for chemical composition using EDX in order to supplement the SIMS data. The results are given in the following sections for the individual samples.

Table 15. Compositions of microstructural constituents in sample 124-95-1 measured by EDX*.

Location	Phase	Al (wt %)	Ni (wt %)	Fe (wt %)	Mn (wt %)	Cu (wt %)
1	α matrix	7.3	3.8	3.8	1.2	83.9
2	5 μm κ_{II}	16.9	21.9	36.1	1.9	23.2
3	globular κ_{II} κ_{III} fingers ~4 μm	13.5	13.9	55.0	1.7	15.9
4	globular κ_{II} with κ_{III} fingers ~2 μm	16.5	22.5	32.0	2.0	27.0
5	globular κ_{II} with κ_{III} fingers ~5 μm	17.7	23.3	30.6	2.2	26.3
6	globular κ_{II} with κ_{III} fingers ~4 μm	18.3	23.2	18.9	2.0	37.6
7	globular κ_{II}, ~4 μm	17.4	24.0	25.1	2.0	31.5
8	κ_{II} boundary phase ~2.5 μm	16.6	23.2	33.7	1.7	24.7
9	κ_{II} attached to κ_{III} fingers ~2.5 μm	17.0	22.7	35.5	1.9	22.9
10	κ_{II} with κ_{III} fingers ~2.5 μm	17.4	23.3	19.2	1.8	38.3

* Expected relative accuracy of 10%

3.12.1 Sample 124-95-1 (Series A1, 9.3% Al, 4.6% Ni, 4.8% Fe)

A total of 10 areas were analyzed in sample 124-95-1 and are indicated in Fig. 42. The results of the analyses are presented in Table 15.

Close examination of Table 15 reveals some interesting trends. A fairly substantial spread in the data is observed for both Fe (18.9-55.0) and Cu (15.9-38.3) for all of the κ_{II} phases analyzed, yet the Ni content remains fairly constant. There does not appear to be any κ_{II} particle size dependence on the concentration.

3.12.2 Sample 124-95-3 (Series A1, 12.5% Al, 4.6% Ni, 4.6% Fe)

A total of six areas were analyzed in sample 124-95-3, with those areas being indicated in Fig. 43. The results of the analyses are given in Table 16. As mentioned earlier, this sample contained numerous relatively fine (2 μm) κ particles both within the α grains and also decorating the prior β boundaries.

Table 16. Compositions of microstructural constituents in sample 124-95-3 measured by EDX*.

Location	Phase	Al (wt %)	Ni (wt %)	Fe (wt %)	Mn (wt %)	Cu (wt %)
1	κ_{II} boundary phase ~2 μm	16.3	15.3	31.8	1.6	34.9
2	κ_{II} boundary phase ~3 μm	17.0	14.0	31.1	1.9	36.0
3	κ_{II} or κ_{III} particles ~2 μm	16.6	14.1	25.2	2.0	42.0
4	κ_{II} or κ_{IV} particles ~2 μm	16.7	15.7	34.0	1.9	31.7
5	α-matrix	11.7	3.0	1.1	1.0	82.2
6	α-matrix with substructure	13.8	3.9	1.3	0.7	80.0

* Expected relative accuracy of 10%

Analysis of the results tabulated above indicates that the main effect caused by the increase in the Al content is an increase in the Al content of the α-matrix. The Al concentration in the κ phases has not been affected by the change in the alloy composition. A slight increase in the Cu content and a decrease in the Ni and Fe contents is observed. However, caution is advised as the size of the particles analyzed in these samples approaches the electron beam/sample interaction volume for X-ray production, and therefore some contributions from the α-matrix may be present in the results.

3.12.3 Sample 136-95-2 (Series A2, 9.3% Al, 4.6% Ni, 6.1% Fe)

Most of the analyses for this sample were taken within a large κ_I rosette showing a coring effect. The areas analyzed are shown in Fig. 44. A total of 10 areas were analyzed, and the results are tabulated in Table 17.

A complex behaviour is observed within the κ_I rosette, whereby the outermost surface is found to be enriched in Ni as compared to the interior. Furthermore, the broken dendritic structure observed within the interior of the rosette was determined to have a composition more representative of the α-matrix. The lighter κ_{II} particle examined at location 6 shows a slightly higher Fe concentration than that observed for the same phase in the previous samples, which may be a result of the higher Fe content of this alloy.

Table 17. Compositions of microstructural constituents in sample 136-95-2 measured by EDX*.

Location	Phase	Al (wt %)	Ni (wt %)	Fe (wt %)	Mn (wt %)	Cu (wt %)
1	α-matrix	7.1	3.4	6.8	1.1	81.6
2	light grey interior of κ_I rosette	12.5	7.4	67.9	1.9	10.3
3	light grey exterior of κ_I rosette	15.1	15.7	53.0	2.0	14.2
4	dark interior of κ_I rosette arm globule	17.0	6.2	56.0	1.4	19.4
5	light grey κ_I rosette arm globule	13.3	9.3	64.7	2.0	10.7
6	light grey κ_{II} particle	15.3	16.7	46.0	1.8	20.3
7	dark κ_{II} particle	30.7	2.6	1.8	0.8	64.0
8	light grey κ_{III} globule	17.9	27.1	15.8	1.8	37.4
9	light arm within κ_I rosette	10.3	2.3	8.5	1.0	77.9
10	dark interior of κ_I rosette	31.0	4.7	53.8	1.4	9.2

* Expected relative accuracy of 10%

3.12.4 Sample 140-95-3 (Series D1, 7.8% Al, 3.7% Ni, 4.4% Fe, 1.12% Cr, 0.79% Ti, 0.68% Zr)

Finally, sample 140-95-3 with additions of all of Cr, Ti and Zr was analyzed to help identify some of the unknown phases encountered in both optical microscopy and SIMS. A total of 11 areas were analyzed (noted in Fig. 45), and the results are presented in Table 18.

Analysis of the above data indicates that Cr has a strong tendency to solidify in the κ_I rosettes, although the range of concentrations can be quite large, extending from 9.6 to 32.0 wt %. High Ti concentrations are noted predominantly in the boundary phases, although an occasional high level is also noted for one κ_I rosette (location 7) and the only κ_{II} particle analyzed (location 11). The same holds true for Zr, which is observed at levels above approximately 1 wt % only in the boundary phase. These results are in good agreement with the qualitative SIMS data.

Table 18. Compositions of microstructural constituents in sample 140-95-3 measured by EDX.

Location	Phase	Al (wt %)	Ni (wt %)	Fe (wt %)	Mn (wt %)	Cu (wt %)	Zr (wt %)	Ti (wt %)	Cr (wt %)
1	α-matrix	6.6	3.3	1.3	1.2	87.2	-0.02	0.1	0.2
2	elongated κ_I 5 x 20 μm	5.1	3.7	48.9	0.5	6.6	0.04	3.2	32.0
3	light grey boundary phase	12.0	26.0	23.5	0.4	14.3	1.2	20.4	2.2
4	white boundary phase	9.6	23.0	2.9	-0.01	28.5	32.1	3.7	0.2
5	globular κ_I or κ_{II}	4.5	1.8	58.1	0.8	5.4	0.3	2.2	26.9
6	light grey boundary phase	11.9	27.2	17.3	0.3	18.9	5.1	17.5	1.7
7	κ_I rosette	11.3	20.6	27.1	0.8	14.9	1.0	14.6	9.6
8	elongated κ_I phase	12.1	24.8	24.0	0.2	15.9	1.0	19.7	2.3
9	grey boundary phase	2.5	3.8	50.0	0.8	4.4	7.1	20.4	10.9
10	κ_I rosette	5.0	4.7	47.5	0.7	7.4	0.7	3.2	30.8
11	globular κ_{II} particle ~5 μm	12.0	25.2	24.0	0.2	15.8	1.3	19.2	2.3

* Expected relative accuracy of 10%

4. DISCUSSION

The results presented pertaining to the C95800 Cu-Al-Fe-Ni alloy are in good agreement with those obtained in previous studies. In general, these complex alloys form by solidification of a high-temperature β phase which subsequently transforms to a face-centered cubic (FCC) solid solution α phase, several unique intermetallic phases (designated κ_I, κ_{II}, κ_{III} and κ_{IV}) and regions of retained β phase. Relatively small compositional variations within these types of alloys can change the sequence of solidification and have a pronounced effect on the resultant microstructure. For alloys with Ni:Fe ratios >1 (Ni-rich) solidification of a body-centered cubic (BCC) β phase occurs, whereas in alloys with Ni:Fe ratios <1 (iron-rich) some κ_I particles are formed from the liquid melt prior to β phase precipitation (4,5,9). In the former case (Ni-rich), when the solubility of Cu in the β phase is reduced, α phase begins to form at the β grain boundaries. In the latter case, (Fe-rich), the κ_I particles continue to grow and become a preferred site for nucleation of α. With continued cooling of the standard alloy, κ_{II} precipitates are nucleated in the β phase shortly after the α phase begins to form. Although the majority of the κ_{II} particles are nucleated near the α/β interface, some may be encapsulated by the growing α phase. On further cooling, the solubility of iron in α is exceeded, and small κ_{IV} particles begin to nucleate and continue to grow. This is followed by the eutectoid reaction, whereby β phase is decomposed to $\alpha + \kappa_{III}$ at the α/β boundaries. The remaining β phase, which has traditionally been referred to as retained β, actually transforms to martensite (6).

With these solidification and solid-state transformation processes in mind, the microstructures of the Al series alloys can be explained. At 9.3 wt %, Al and the Ni and Fe contents given in Table 4, insufficient Fe was present to form the κ_I rosettes. However, on further cooling, κ_{II} and κ_{III} phases did precipitate at the β boundaries, and some retained β phase can be observed surrounded by the two κ phases. The κ_{IV} phase has precipitated within the α-grains as expected.

Increasing the Al content to 10.7 wt % produces two effects: it tends to stabilize the β phase to lower temperatures, and the κ phases are now precipitated directly from the β phase. This is observed in the microstructures whereby the κ_{II} phase is uniformly distributed throughout both the α and retained β phases. Similar results are observed when the Al content is raised to 12.5 wt %. In this case, the precipitation of the κ_{II} particles at the prior β boundaries is quite evident.

In the A2 series of alloys, excess Fe was added (~6.2 wt %), lowering the Ni/Fe ratio to 0.74, and the effect of increasing Al content was studied. At 8.8 wt % Al, all phases, with the exception of retained β, can be observed. The κ_I rosettes are observed within the central portions of the α-grains. They tend to be surrounded by the Ni-rich κ_{III} phase as would be expected from the local enrichment of Ni produced by the formation of κ_I. Furthermore, the EDX results

indicated that the outermost surface of the κ_I rosette was also Ni-rich, supporting the theory of a local enrichment of Ni.

The main effect of increasing the Al content to 9.3 and then to 9.7 wt % is twofold. First, more retained β is observed in the microstructure, as might be expected. Second, the volume fraction of the κ_I phase seems to have decreased, suggesting that the solubility of Fe in the melt has increased with Al content assuming that the κ_I phase precipitates directly from the melt (4,5,9).

For the B1 alloy series, the effect of changing the Ni/Fe ratio at a constant Al content of 9.2 wt % was studied. For sample 128-95-1, with Ni and Fe contents of 5.0 and 4.7 wt % respectively, the effect of the slight Ni enrichment is to produce a microstructure with an abundance of κ_{III} phase. No κ_I rosettes are formed, and some retained β phase can be observed.

Increasing the Ni content to 6.5 wt % while leaving the Fe concentration at 4.7 wt % produces an extreme abundance of the κ_{III} phase. Finally, if both the Ni and Fe levels are increased, as in sample 128-95-3, the resulting microstructure shows an abundance of both κ_{II} and κ_{III}. Interestingly, no κ_I was formed, possibly because the critical Fe content had not been reached. Comparing this alloy series with the A2 series implies that the critical concentration must lie somewhere between 5.7 and 6.2 wt % for this Al content.

When the Al concentration is raised to 10.1 wt %, as in the series B2 alloys, and the Ni and Fe levels are held at slightly below 4 wt %, the structure consists of roughly equal proportions of retained β and α-grains, and predominantly κ_{II} and κ_{III} precipitates. These precipitates are located at the periphery of the α-grains, indicating that they formed after the α-grains and precipitated at the α/β interface.

Increasing the Fe content to 5.5 wt % produces two effects: it includes the formation of κ_I rosettes and stabilizes the α-grain structure. Although a great deal of retained β phase is still present in sample 125-95-3, the volume fraction of α/β phase is higher in this sample compared to the previous sample.

As might be expected from analysis of previous samples, when the Al content is further raised to 11.3 wt %, and the Ni and Fe concentrations are roughly 4 wt %, as in sample 132-95-1, a significant portion of retained β and the prior β boundaries are clearly observable. The microstructure is also uniformly distributed with κ_{II} particles, indicating that they began precipitating prior to the α-grains.

Increasing the Fe content to 5.0 wt %, as in sample 132-95-2, leads to little change in the microstructure and a further increase to 5.8 wt %, as in sample 132-95-3, produces only two notable differences in the microstructure. First, the size of the prior β grains seems to have decreased, and secondly, the κ_{II} particles appear to have coarsened, and occupy a greater volume fraction of the microstructure. The reason for the decrease in the prior β grain size can be rationalized based on these observations. At relatively low Ni and Fe concentrations, as in the

previous two samples, these elements are able to remain in solid solution in the β phase to lower temperatures than for sample 132-95-3. However, at higher Ni and Fe concentrations, the solid solubility range is exceeded at higher temperature, resulting in the precipitation of κ_{II} particles. These particles can effectively pin grain boundaries from migration, and as a result, β grain growth will be inhibited. This yields the end result of smaller prior β boundaries.

The effect of a final increase in the Al content to 12.2 wt % was studied in the series B4 alloys. The results were found to be very similar to the B3 alloys, and the same trends were observed. Interestingly, the sample with the highest Ni and Fe levels again showed the smaller prior β grain size. The fact that the prior β boundaries are also observed to be decorated with κ_{IV} would suggest that the pinning mechanism described above is indeed operating. Although this sample contains a high Fe content, no κ_I phase was observed. The reason for this is attributed to an increase in the solubility of Fe in the melt as a consequence of the high Al content postulated from the results obtained for the A2 alloy series.

For the series C1 alloys, the effect of Cr additions on the microstructure was investigated. At an Al concentration of 9.6 wt % and Ni and Fe levels of 5.2 and 4.8 wt %, respectively, a 0.61 wt % addition of Cr, as in sample 137-95-1 does not produce any striking differences in the microstructure. Columnar α-grains are observed containing all four κ phases, with the most abundant being κ_{III}. Given the Ni/Fe ratio in this sample, this does not come as a surprise.

If the Fe and Cr levels are increased to 5.6 and 1.15 wt % respectively, an increase in the amount of the κ_I phase, seemingly at the expense of the κ_{III} phase, is observed. SIMS direct ion images from this sample verified that Cr was mainly present in the κ_I phase, indicating that its solid solubility in the melt is quite limited. Continuing growth of the α-grains therefore contains these initial κ_I precipitates in their grain interiors. A further increase in the Fe and Cr content, as in sample 137-95-3, leads to more dramatic examples of this effect.

The effect of Ti additions was studied in the series C2 alloys, and for an alloy with 10.0 wt % Al, 5.0 wt % Ni, 6.3 wt % Fe and 1.08 wt % Ti, an equiaxed α-grain structure containing significant amounts of κ_I, κ_{II} and κ_{IV} phases was noted. Thus, it is concluded that Ti prevents the formation of the κ_{III} phase. SIMS direct ion images from this sample indicated that these κ_I rosettes were rich in all of Fe, Ni and Ti. This suggests that the addition of Ti has decreased the solid solubility of all elements in the melt. Indeed, an examination of the binary Ni-Ti phase diagram reveals a series of intermetallic compounds, and therefore it may be hypothesized that Ti assists in bringing Ni to the Fe-rich κ_I phase. This is confirmed by two further additions of Ti, whereby rapid increases in the size of the κ_I rosettes were observed. These increases apparently come at the expense of all other κ phases.

Finally, in the C3 series alloys, the effect of a 0.97 wt % Zr addition was investigated. The results were similar to those obtained for Ti, whereby equiaxed α-grains were present, combined with all κ phases, as well as an unknown needle-like phase. SIMS direct ion images

indicated that the κ_1 rosettes were indeed rich in Fe but contained very little Zr. However, the needle-like phase observed in the optical micrographs was found to be rich in Zr.

The effect of adding all of Cr, Ti and Zr was investigated in the series D1 alloys. At low levels of the three alloying elements, as in sample 140-95-1, all four κ phases are observed within the α-matrix, and the needle-like phase mentioned above is occasionally observed. As the Cr, Ti and Zr levels are increased further, the κ_1 particles coarsen, and some unknown grain boundary phase evolves. One final increase in the Cr, Ti and Zr levels leads to an abundance of κ_1, the needle-like phase and the grain boundary phase. The needle-like phases appear centrally located within the α-grains, indicating that they precipitated out of solution at approximately the same temperature as the like-situated κ_1 rosettes. These rosettes were rich in Ti, Fe and Cr. The boundary phase, on the other hand, is rich in all of Ti, Fe, Cr and Zr, and must have been amongst the last phases to precipitate. This would also explain the variation in the SEM/EDS determined concentrations, where large changes in composition along the particular phase were noted.

Since the retained β phase is observed even at a low Al content of 7.8 wt % (sample 140-95-3), it is evident that the equivalent aluminum content has increased due to the presence of all three modifying elements (i.e. Cr, Ti and Zr). Also, the amount of retained β is high even at Al contents of 9.3 wt % (sample 140-95-1) and 8.9 wt % (sample 140-95-2) when compared with samples of similar composition but without the modifying elements (i.e. samples 124-95-1 and 136-95-1, respectively).

5. CONCLUSIONS

The main conclusions which can be drawn from this report can be divided into two categories: those pertaining to the results generated from the standard alloy chemistries, and those generated from the alloys with additions of Cr, Ti and Zr, either singly or in combination.

The results from the alloys with the standard chemistries are in good agreement with those found in the literature, and illustrate how sensitive the resulting microstructure is to the alloy chemistry. In particular, variations of the order of one-half a percent or less of Al have profound effects on the microstructure. These changes in the microstructure will obviously affect the mechanical and corrosion properties of the material, and so great care must be exercised in controlling the alloy chemistry for a desired application. Indeed, large variations in the microhardness for relatively small changes in chemistry were already determined in this study.

Additions of Cr and Ti to the standard alloy chemistry led to these elements precipitating as large rosettes to form initially. Observations by SIMS of high secondary ion intensities of these elements in the κ_I rosettes led to this conclusion. Additions of Ti were also found to prevent the formation of the κ_{III} phase. On the other hand, the effect of a Zr addition was the formation of a needle-like, Zr-enriched phase. The exact identification and crystallography of this phase is as yet undetermined. The addition of all three modifying elements was found to have the effect of increasing the effective Al content.

The characterization of the complex microstructures formed in the alloys with additions of Cr, Ti and Zr has revealed some of the deficiencies in the current scheme used to describe the various κ phases. With this scheme it is difficult in some cases to discriminate between the various κ phases particles and fails to accommodate the complex Cr, Ti and Zr particles.

6. RECOMMENDATIONS FOR FUTURE WORK

The complex microstructures formed in a series of experimental NAB alloys, designed to provide a systematic study of alloy composition, have been characterized in terms of their as-cast microstructure, morphology, composition and resultant microhardness. To extend this work to assist with interpretation of results from on-going investigations being conducted at DREA, the following work is proposed for a select group of the experimental alloys:

1. Establish a more complete understanding of the morphological and chemical nature of the κ precipitates present in the various alloys using transmission electron microscopy. This would be of particular value for those precipitates with dimensions less than 1-2 μm in size, as the effect of beam spreading on X-ray emission can be avoided using thin specimens. Furthermore, electron diffraction could be employed to determine the crystallographic nature of the precipitates, and especially the unknown Zr-enriched phase.

2. Use Gleeble simulation techniques to determine the microstructural modifications that would be expected to occur in both weld metal and HAZ regions for cooling times associated with the range of laser parameters used in the surface melting experiments.

3. Provide samples of known thermal history for supplementary erosion and corrosion evaluations.

7. ACKNOWLEDGMENTS

The authors wish to thank Dr. Calvin Hyatt, Defence Research Establishment Atlantic for supporting this project and for many fruitful discussions. They also gratefully appreciate the assistance of Dr. F. Fasoyinu and the staff of the experimental casting laboratory for preparing the series of experimental NAB castings as well as Mr. B. Casault for his technical assistance with the SEM analysis and Mrs. C. Bibby for assisting with the optical metallography. The technical support of Mr. V. Chartrand in the SIMS laboratory is also gratefully acknowledged.

8. REFERENCES

1. C.V. Hyatt and K.H. Magee, "Laser surface melting and cladding of nickel aluminum bronzes", in *Proceedings of Advanced Methods of Joining New Materials II,* The American Welding Society, Miami, Florida (1994) pp. 111-126.

2. J.A. Gianetto, M. Sahoo, M.W. Letts and C. Bibby, "The microstructural characterization of NiAl bronze weldments", *DREA Report CR/95/435,* Defence Research Establishment Atlantic, Dartmouth, Nova Scotia (1995).

3. E.A. Culpan and G. Rose, "Microstructural characterization of cast nickel aluminum bronze" *J Mater Sci.,* 13 (1978) pp. 1647-1656.

4. P. Brezina, "Heat treatment of complex aluminum bronzes" *Int. Metals Review,* 27 (1982) pp. 77-120.

5. P. Weill-Couly and D. Arnaud, "Influence de la composition et de la structure des cupro-aluminiums sur leur comportement en service" *Fonderie,* 322 (1973) pp. 123-135.

6 F. Hasan, A. Jahanafrooz, G.W. Lorimer and N. Ridley, "The morphology, crystallography and chemsitry of phases in as-cast nickel-aluminum bronze" *Met. Trans.,* 13A (1982) pp. 1337-1345.

7. R. Thomson and J.O. Edwards, "The kappa phase in nickel-aluminum bronze, Part 1: Slow-cooled microstructures", in *proceedings of the 82nd Annual Meeting of the American Foundryman's Society* (1978) pp. 385-394.

8. M. Sahoo, J.O. Edwards and R. Thomson, "Influence of Corrosion-Inhibiting Heat Treatment on the Microstructure,Impact and Fatigue Properties of Nickel-Aluminum Bronze Alloy C95800", *Trans American Foundryman's Society* 88 (1980) pp. 769-776.

9. Jahanafrooz, A., Hason, F., Lorimer, G.W. and Ridley, N. "Microstructural development in complex nickel-aluminum bronzes", Metall. Trans., Vol. 14A, No. 10, p. 1951-56, 1983.

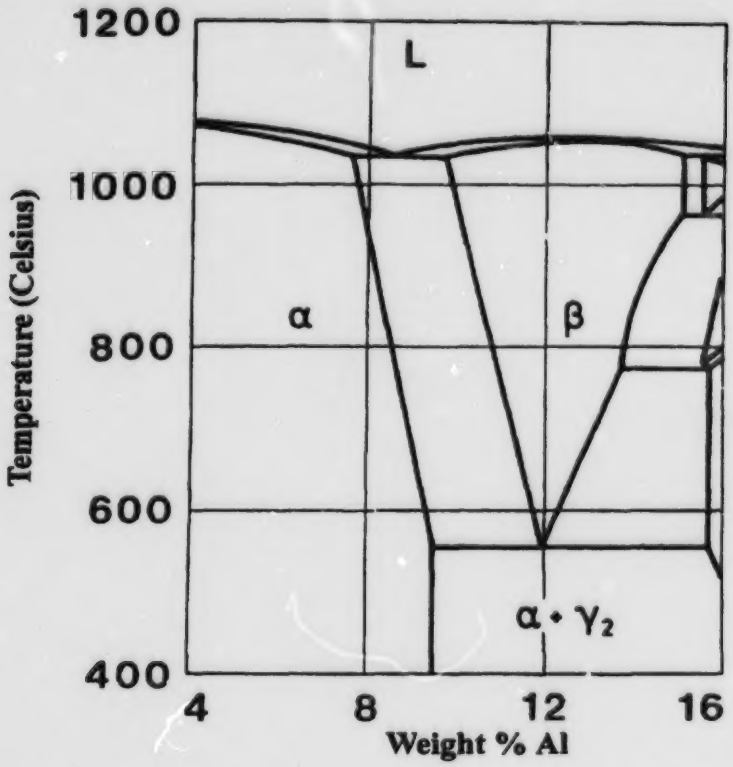

Fig. 1. Binary Cu-Al phase diagram (4).

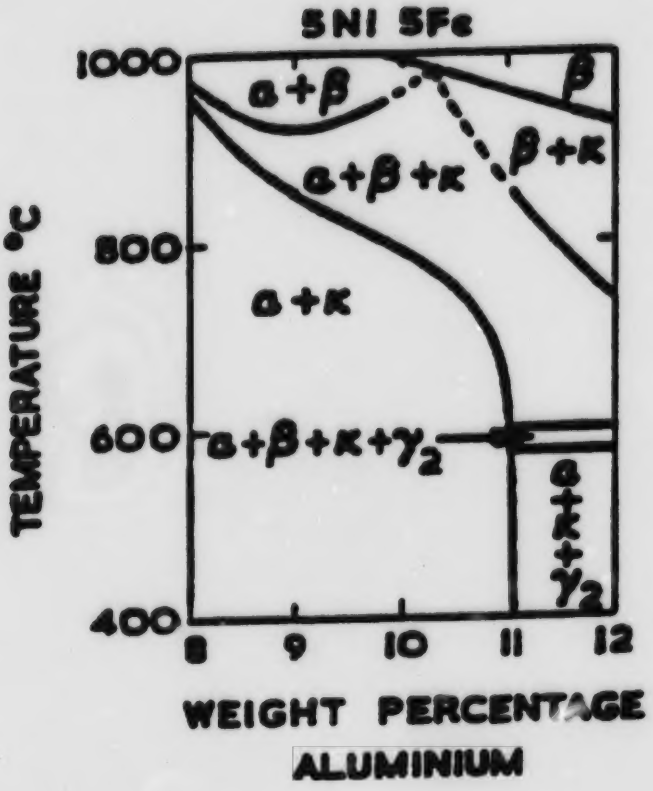

Fig. 2. Section of the quaternary Cu-Al-Fe-Ni phase diagram for 5 wt.% Ni and 5 wt.% Fe (3).

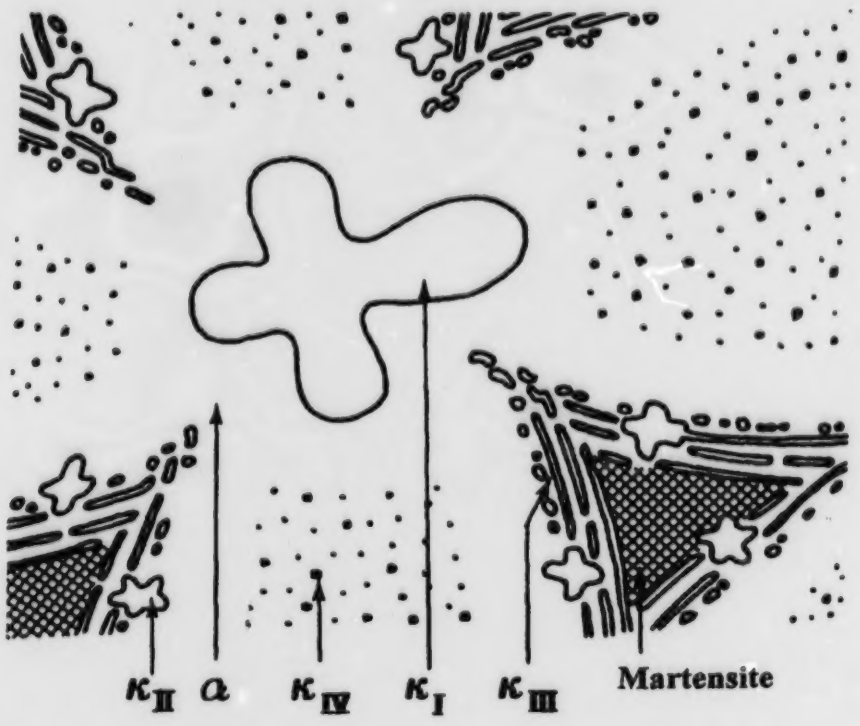

Fig. 3. Schematic representation of phases in typical NAB alloys (6).

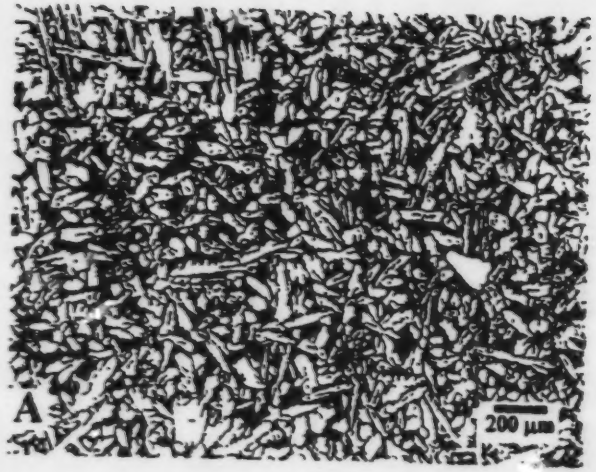

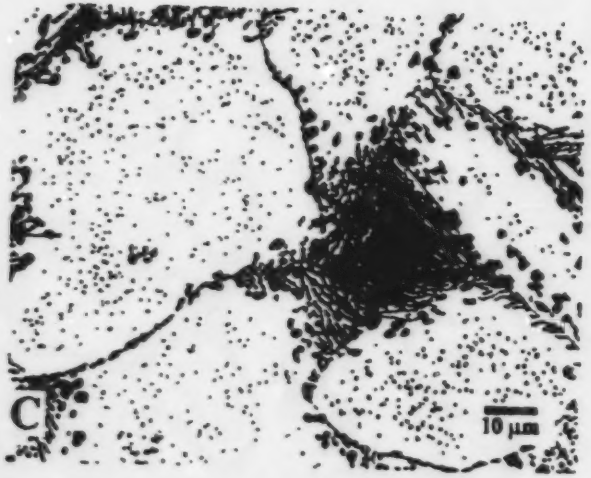

Fig. 4. Optical micrographs of sample 124-95-1 (9.3% Al, 4.6% Ni, 4.8% Fe) from series A1 showing columnar α grains and κ_{II}, κ_{III} and κ_{IV} phases. Some dark-etching retained β phase is also observed.

CANMET

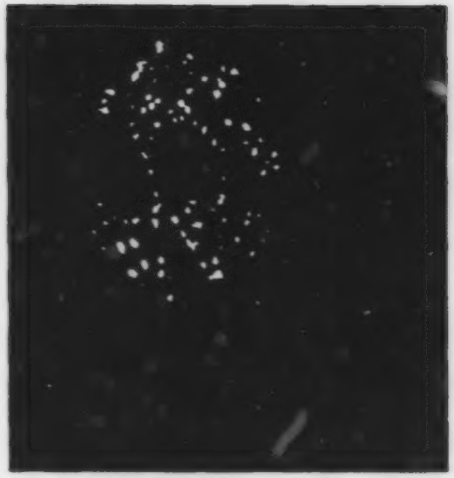

(a)

(b)

(c)

Fig. 5. SIMS direct ion images from sample 124-95-1 for (a) Fe, (b) Ni and (c) Cu. The Fe, and to a lesser extent Ni, enrichment of the κ_{II} phase is clear. The field of view is 100 μm.

CANMET

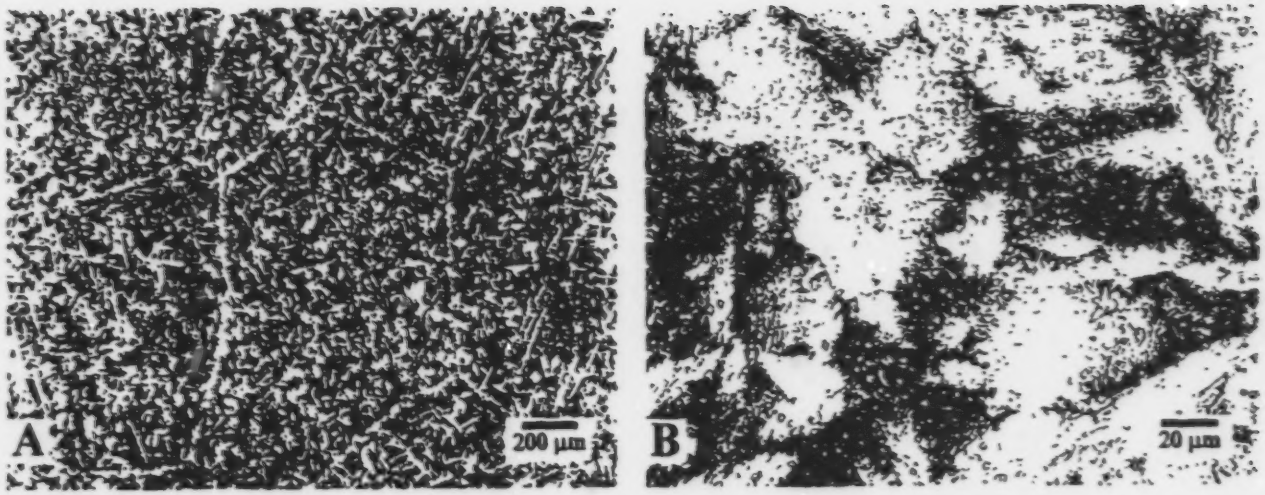

Fig. 6. Optical micrographs of sample 124-95-2 (10.7% Al, 4.7% Ni, 4.7% Fe). (a) low magnification showing prior β boundaries and (b) higher magnification where κ_{II} and κ_{IV} phases are observed.

CANMET

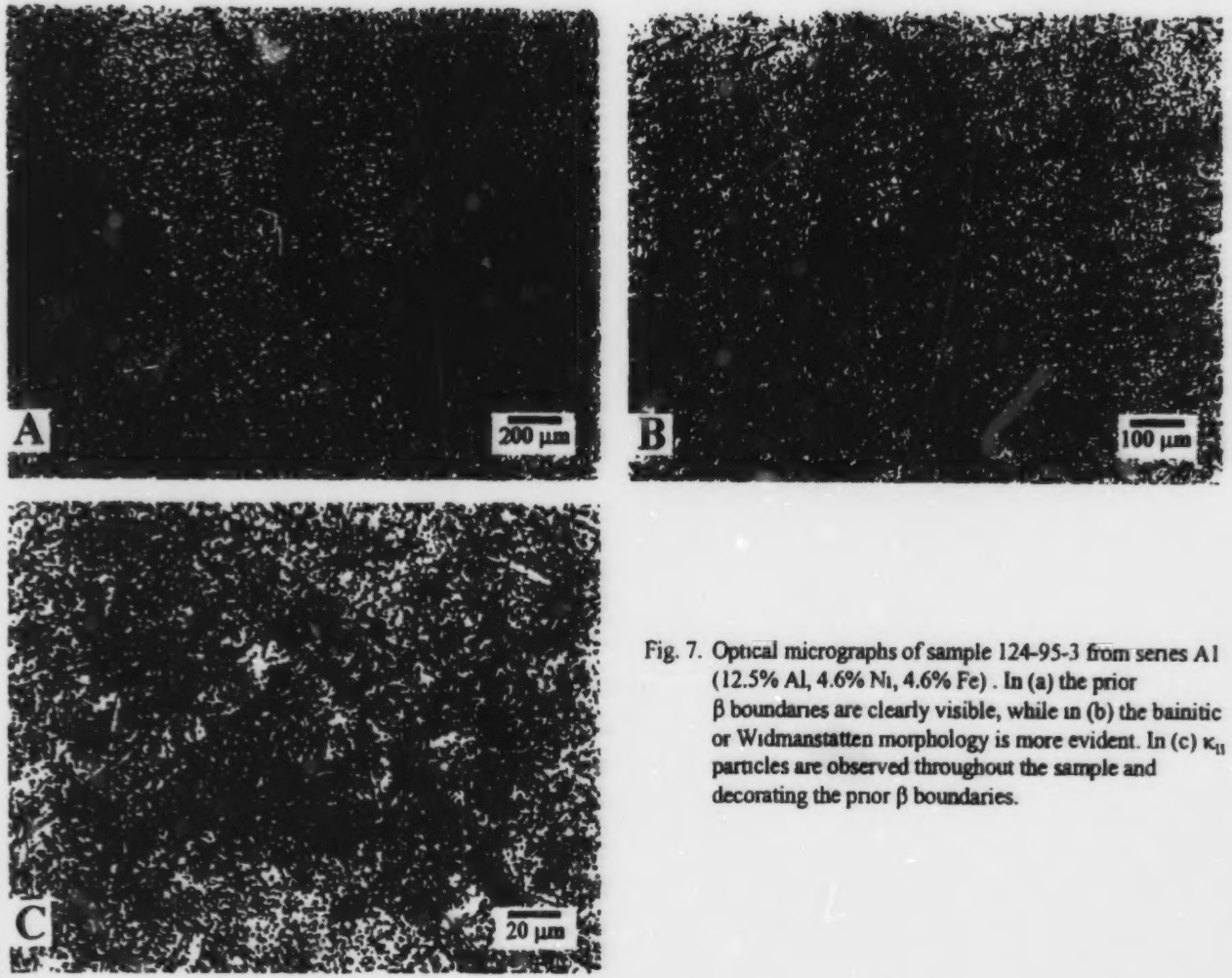

Fig. 7. Optical micrographs of sample 124-95-3 from series A1 (12.5% Al, 4.6% Ni, 4.6% Fe) . In (a) the prior β boundaries are clearly visible, while in (b) the bainitic or Widmanstatten morphology is more evident. In (c) κ_{II} particles are observed throughout the sample and decorating the prior β boundaries.

CANMET

Fig. 8. SIMS direct ion images from sample 124-95-3 for (a) Fe and (b) Ni. Note the Fe and Ni enriched κ_{II} phase decorating the grain boundary. The field of view is 100 μm.

CANMET

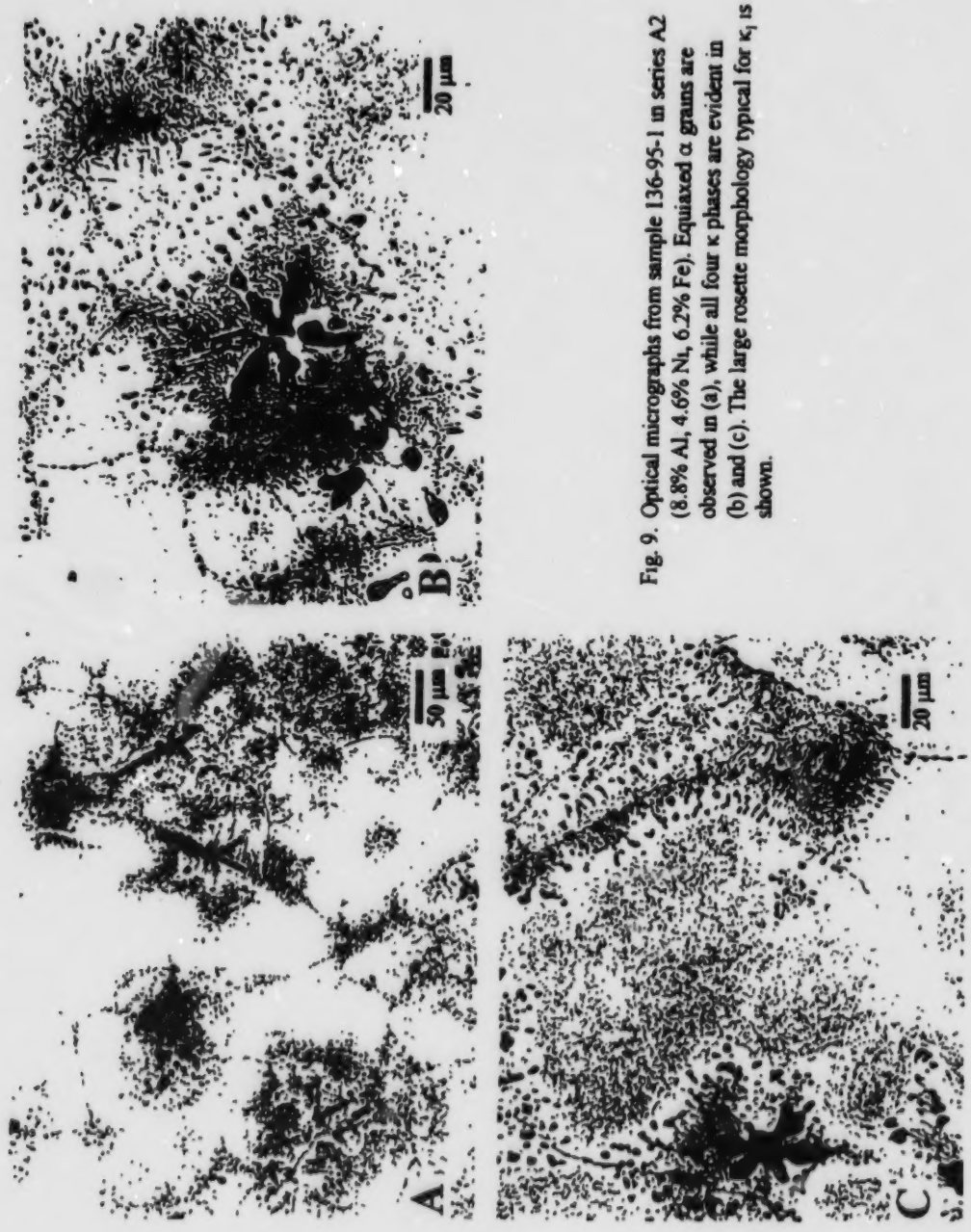

Fig. 9. Optical micrographs from sample 136-95-1 in series A2 (8.8% Al, 4.6% Ni, 6.2% Fe). Equiaxed α grains are observed in (a), while all four κ phases are evident in (b) and (c). The large rosette morphology typical for κ_1 is shown.

Fig. 10. Optical micrographs for sample 136-95-2 from series A2 (9.3% Al, 4.6% Ni, 6.1% Fe) . Note the slightly more columnar-like appearance of the α grains in (a). All four κ phases are again observed in (b).

CANMET

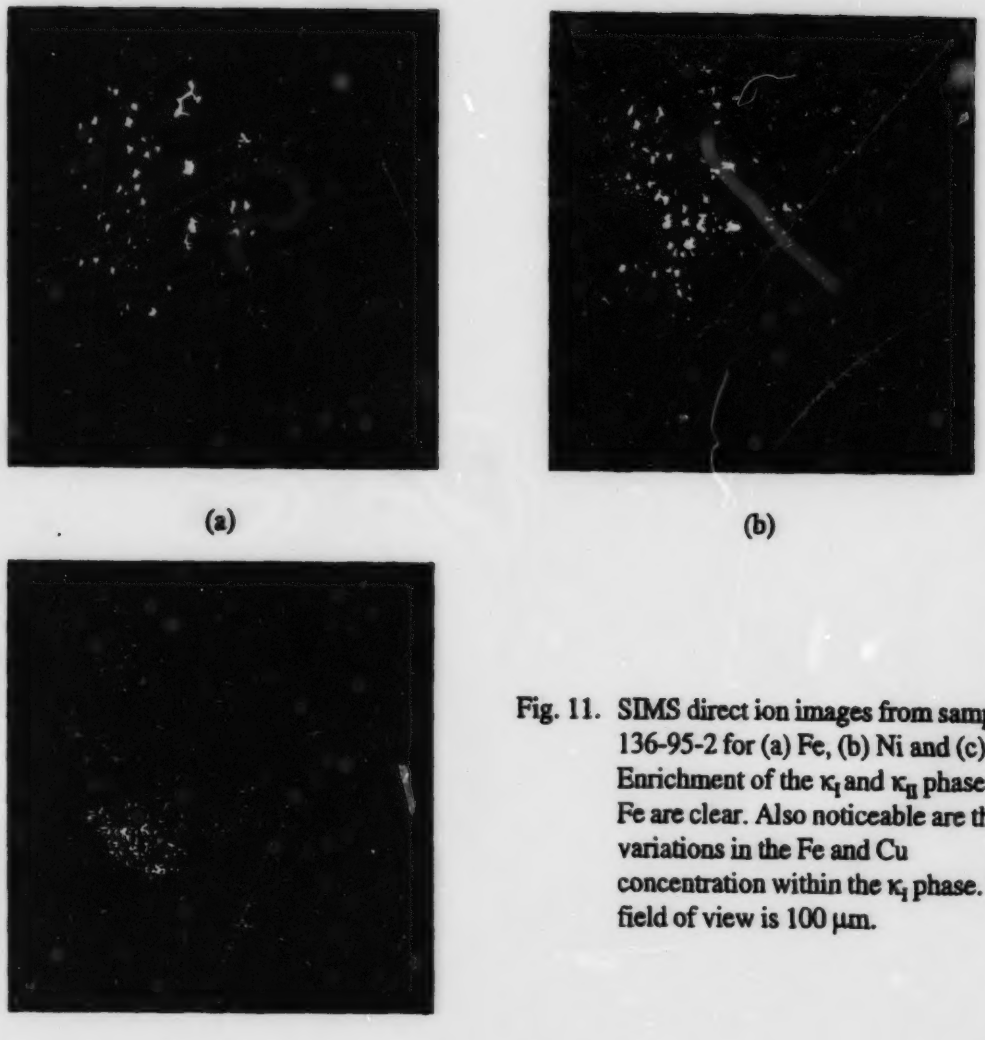

Fig. 11. SIMS direct ion images from sample 136-95-2 for (a) Fe, (b) Ni and (c) Cu. Enrichment of the κ_I and κ_{II} phase in Fe are clear. Also noticeable are the variations in the Fe and Cu concentration within the κ_I phase. The field of view is 100 μm.

CANMET

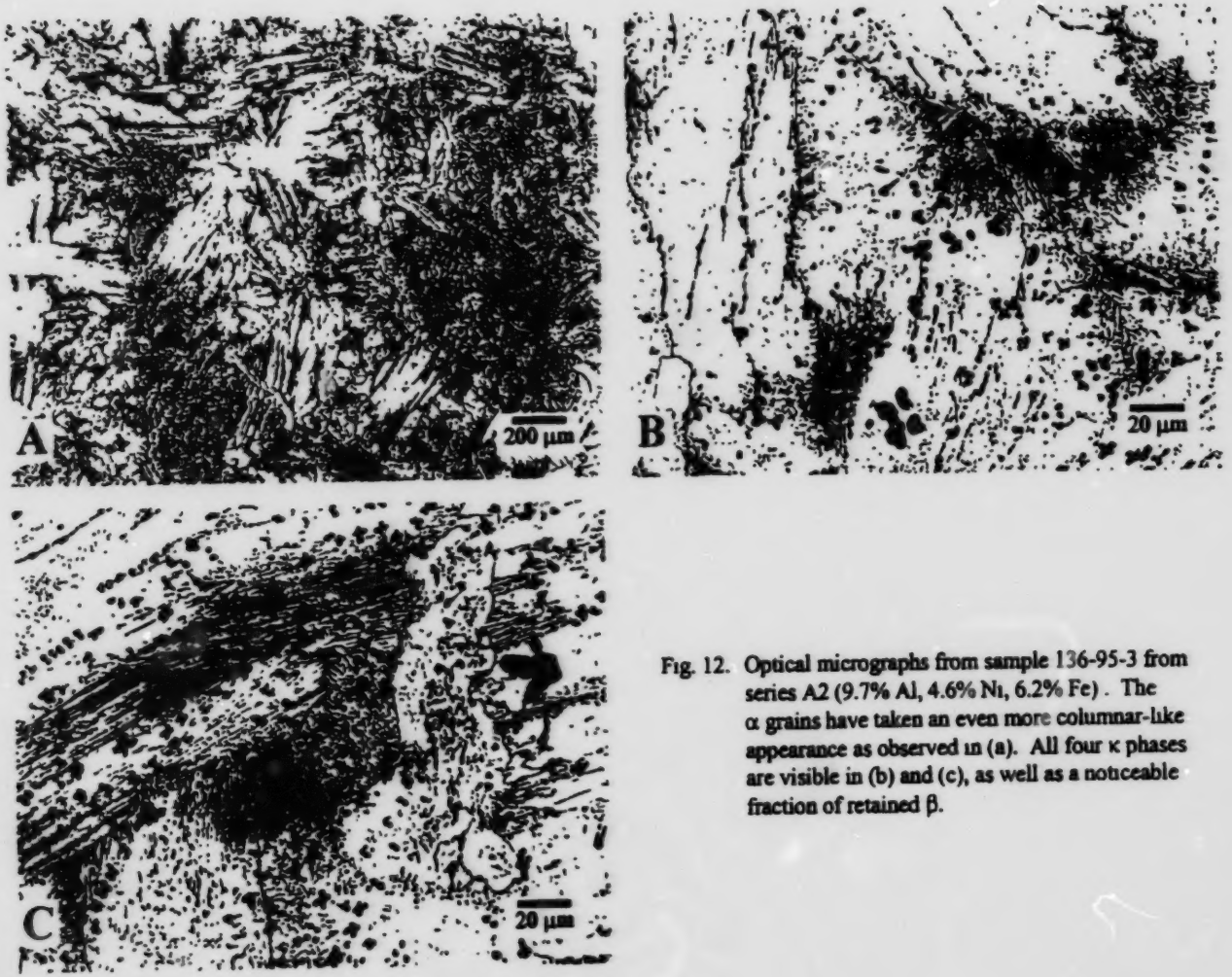

Fig. 12. Optical micrographs from sample 136-95-3 from series A2 (9.7% Al, 4.6% Ni, 6.2% Fe). The α grains have taken an even more columnar-like appearance as observed in (a). All four κ phases are visible in (b) and (c), as well as a noticeable fraction of retained β.

CANMET

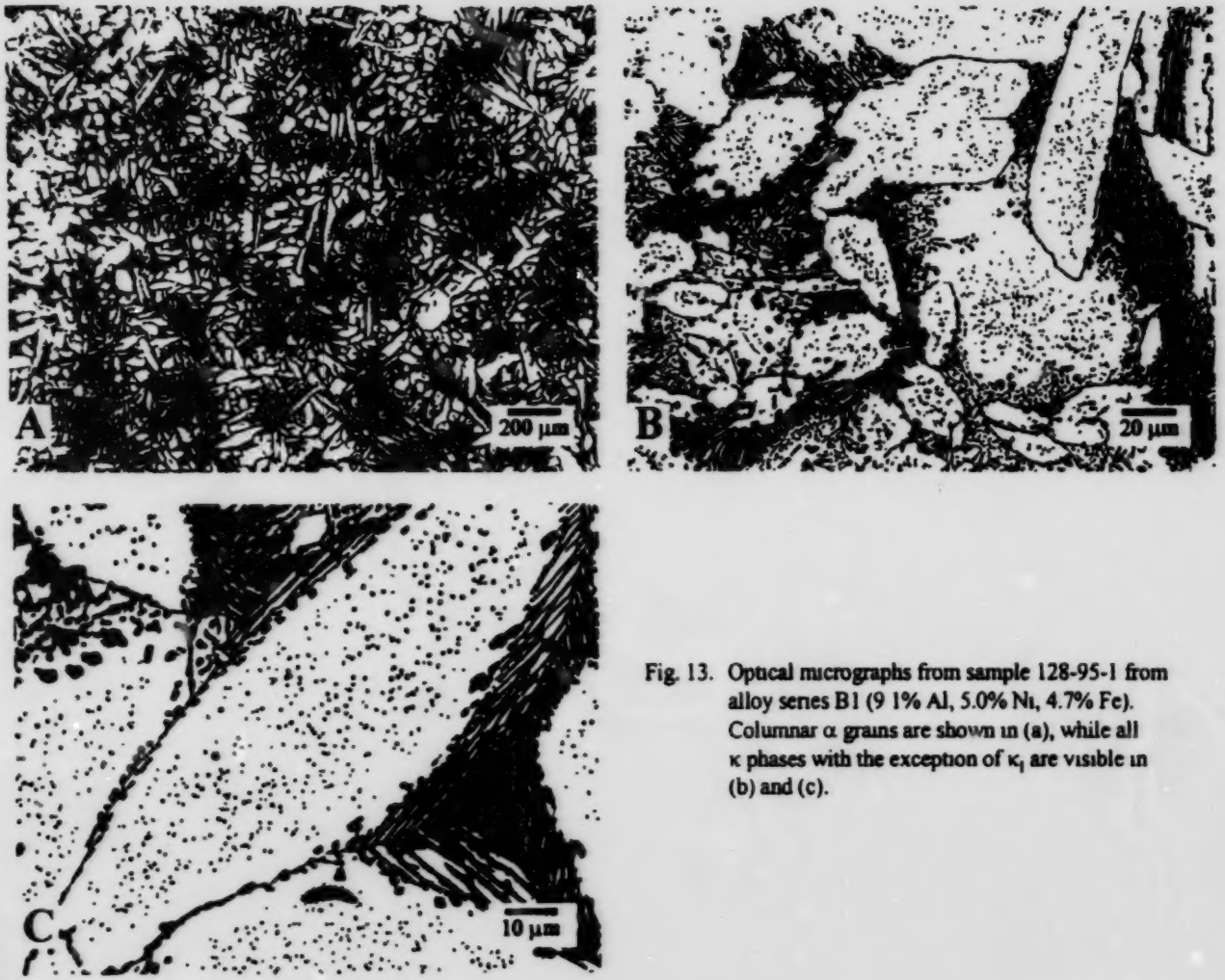

Fig. 13. Optical micrographs from sample 128-95-1 from alloy series B1 (9.1% Al, 5.0% Ni, 4.7% Fe). Columnar α grains are shown in (a), while all κ phases with the exception of κ_I are visible in (b) and (c).

CANMET

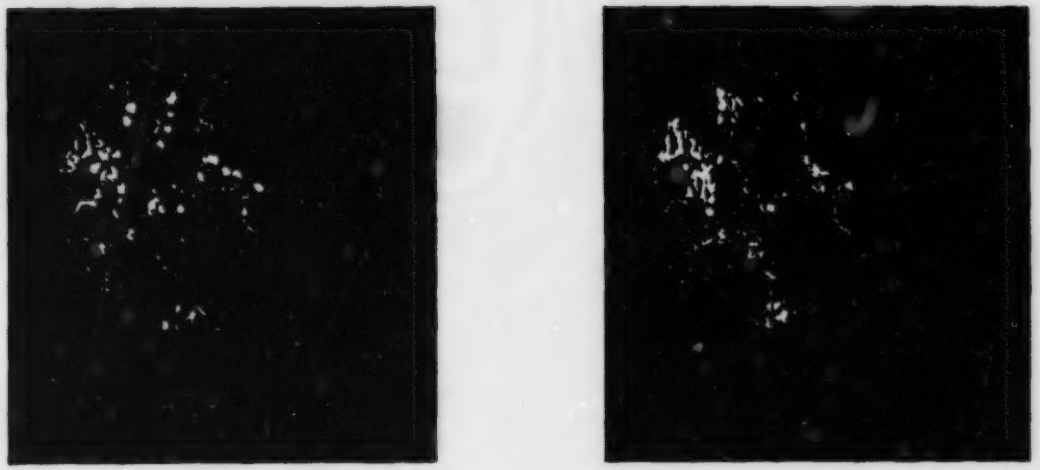

(a) (b)

Fig. 14. SIMS direct ion images for sample 128-95-1 for (a) Fe and (b) Ni. The enrichment of Fe in the κ_{II} phase and to a lesser extent in the κ_{III} phase, as well as the Ni enrichment in the κ_{III} phase, is evident. The field of view is 100 μm.

CANMET

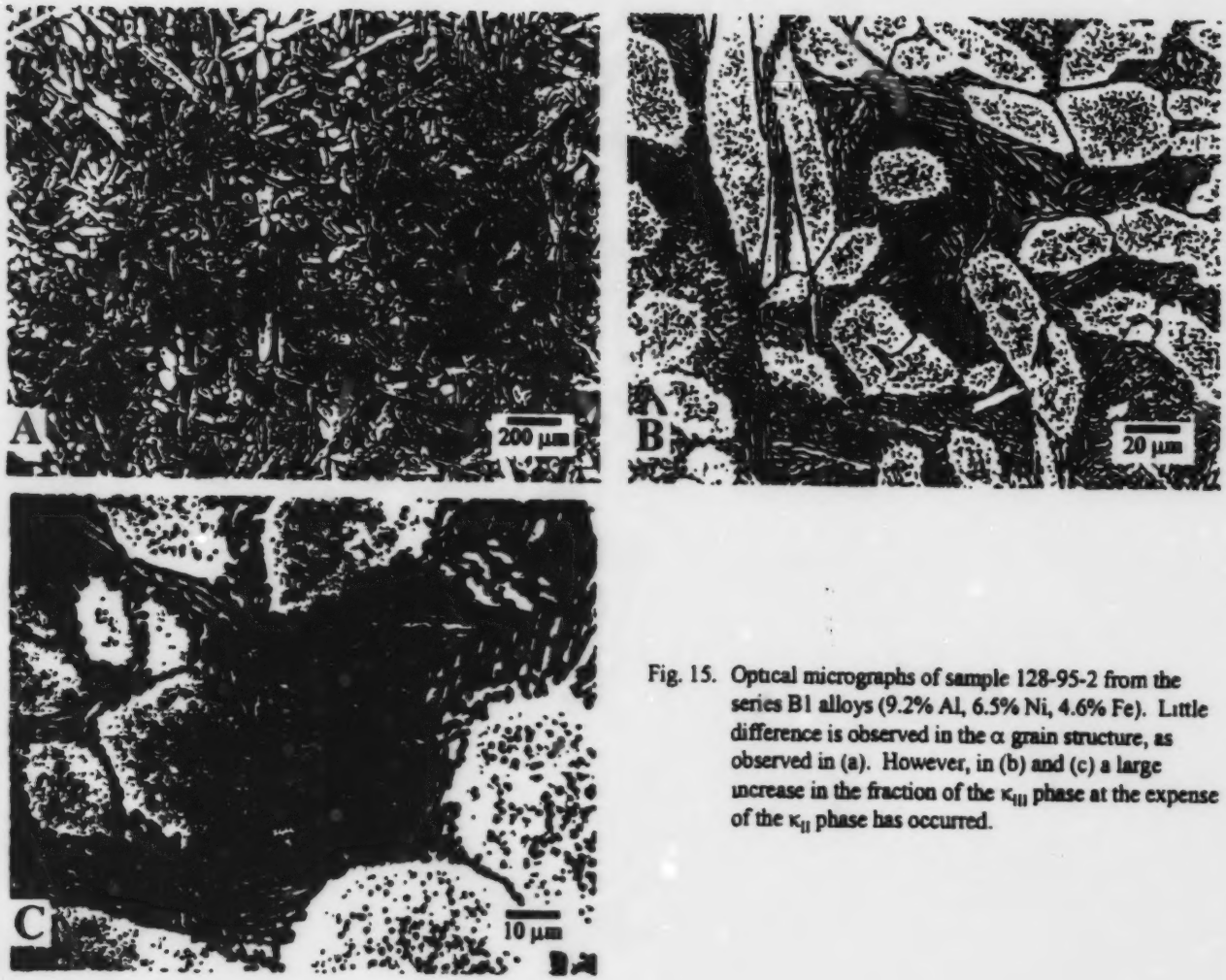

Fig. 15. Optical micrographs of sample 128-95-2 from the series B1 alloys (9.2% Al, 6.5% Ni, 4.6% Fe). Little difference is observed in the α grain structure, as observed in (a). However, in (b) and (c) a large increase in the fraction of the κ_{III} phase at the expense of the κ_{II} phase has occurred.

CANMET

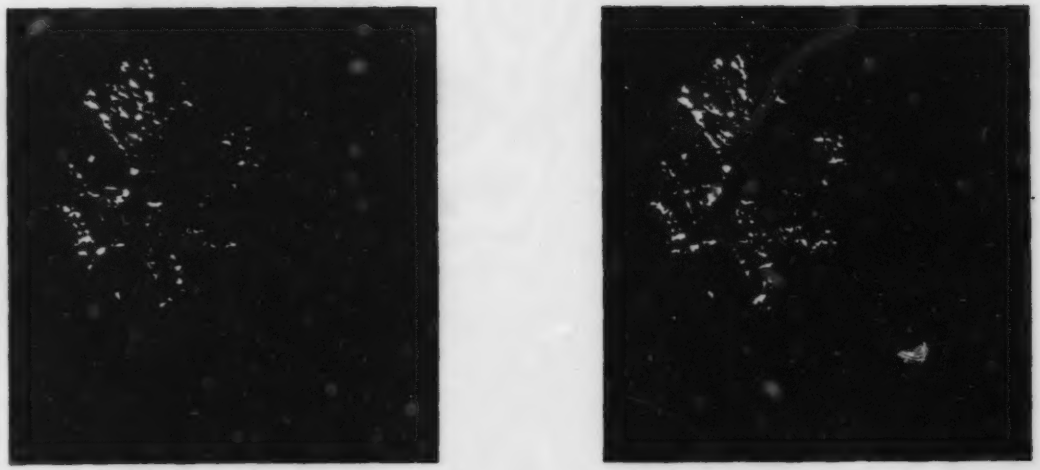

(a) (b)

Fig. 16. SIMS direct ion images for sample 128-95-2 for (a) Fe and (b) Ni. The enrichment of Fe and Ni in the κ_{III} phase is evident. The field of view is 100 μm.

CANMET

Fig. 17. Optical micrographs of sample 128-95-3 from the series B1 alloys (9.2% Al, 6.5% Ni, 5.7% Fe) . The α grains are seen to retain their columnar-like structure in (a), while in (b) a return of the κ_{II} phase at the expense of the amount of the κ_{III} phase has occurred.

CANMET

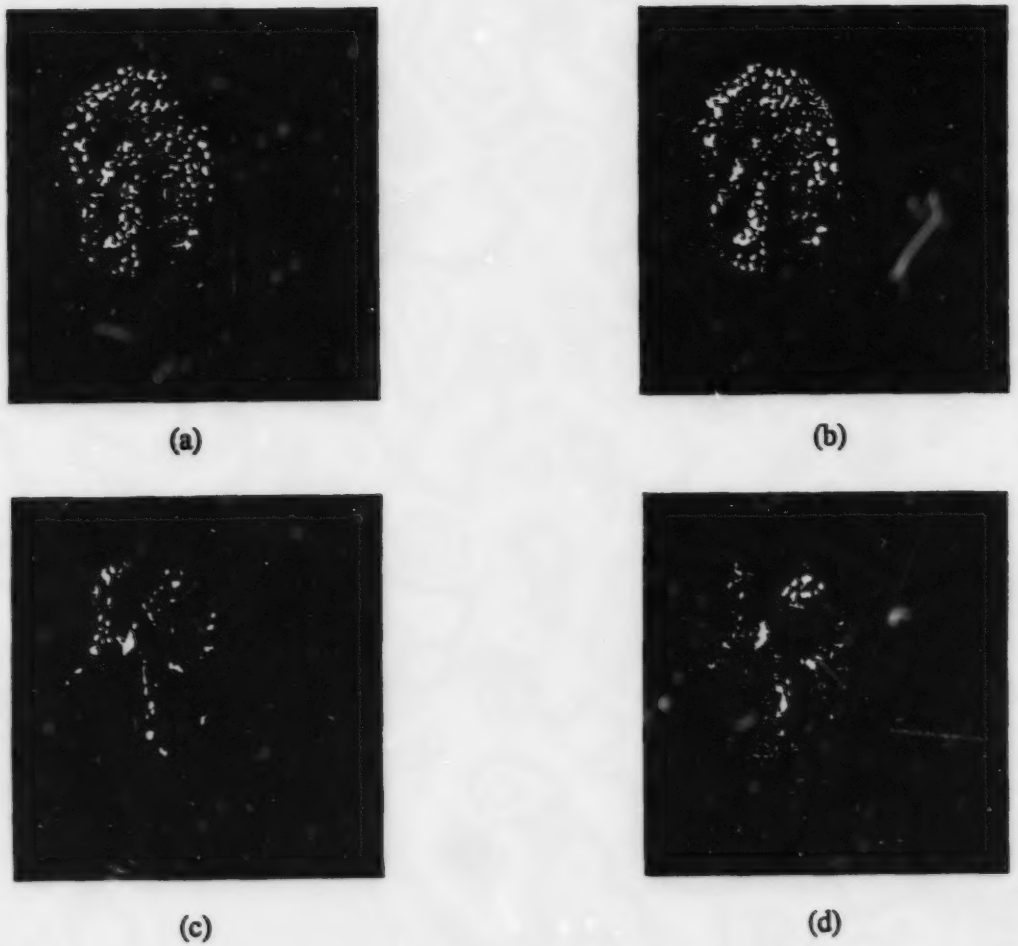

Fig. 18. SIMS direct ion images from sample 128-95-3 for (a) Fe and (b) Ni indicating enrichment of the κ_{III} phase in these elements. Images from a second region for (c) Fe and (d) Ni show a substantial enrichment of Ni in the κ_{II} particles. The field of view is 100 μm.

CANMET

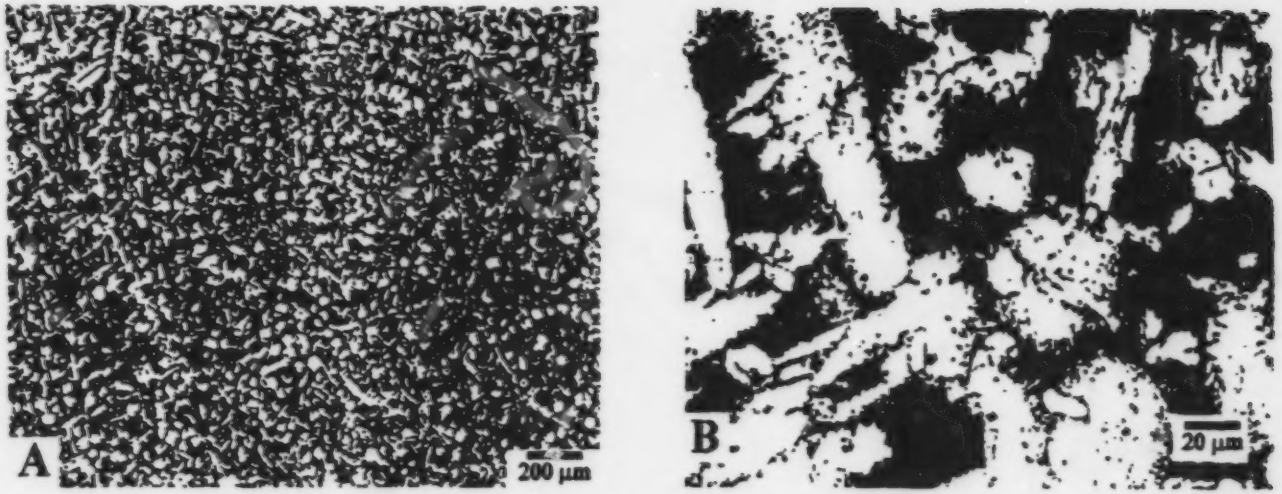

Fig. 19. Optical micrograph of sample 125-95-1 from alloy series B2 (10.1% Al, 3.8% Ni, 3.9% Fe). A mixture of columnar and acicular α grains are observed in (a), while all κ phases with the exception of κ_I are observed in (b). A significant portion of retained β can also be seen in (b).

CANMET

Fig. 20. Optical micrographs of sample 125-95-3 from alloy series B2 (10.1% Al, 3.8% Ni, 5.5% Fe). A more columnar-like appearance of the α grains is noted in (a). A significant portion of retained β is evident in (b), as well as a coarsening of the κ_{II} phase to take on more of a rosette-like morphology.

CANMET

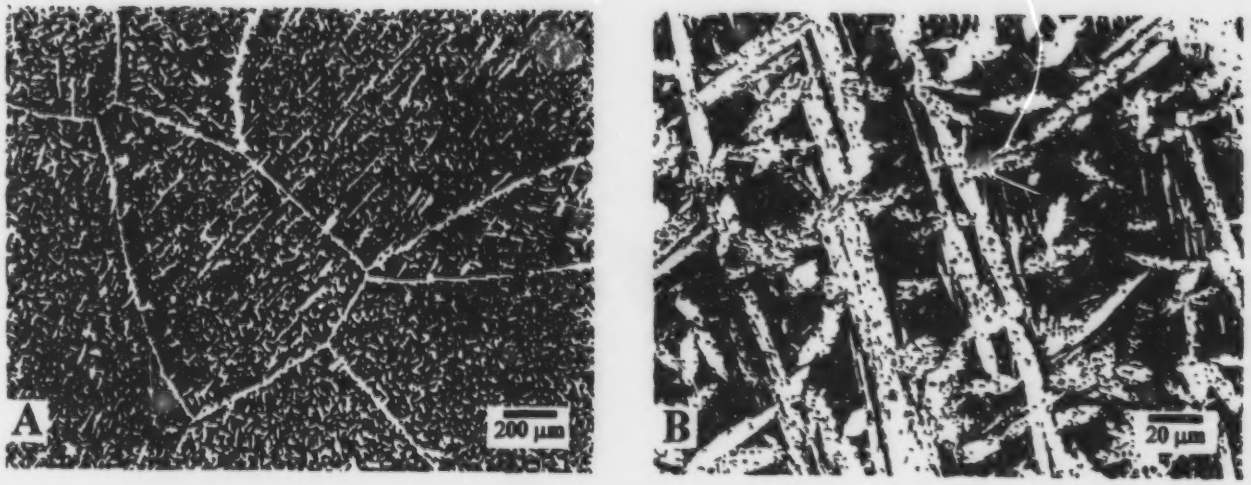

Fig. 21. Optical micrographs of sample 132-95-1 from alloy series B3 (11.3% Al, 4.1% Ni, 4.3% Fe). The prior β boundaries are clearly shown in (a), while in (b) the α grains are observed to be acicular and form a lath-like structure. Many κ_{II} particles are also evident.

CANMET

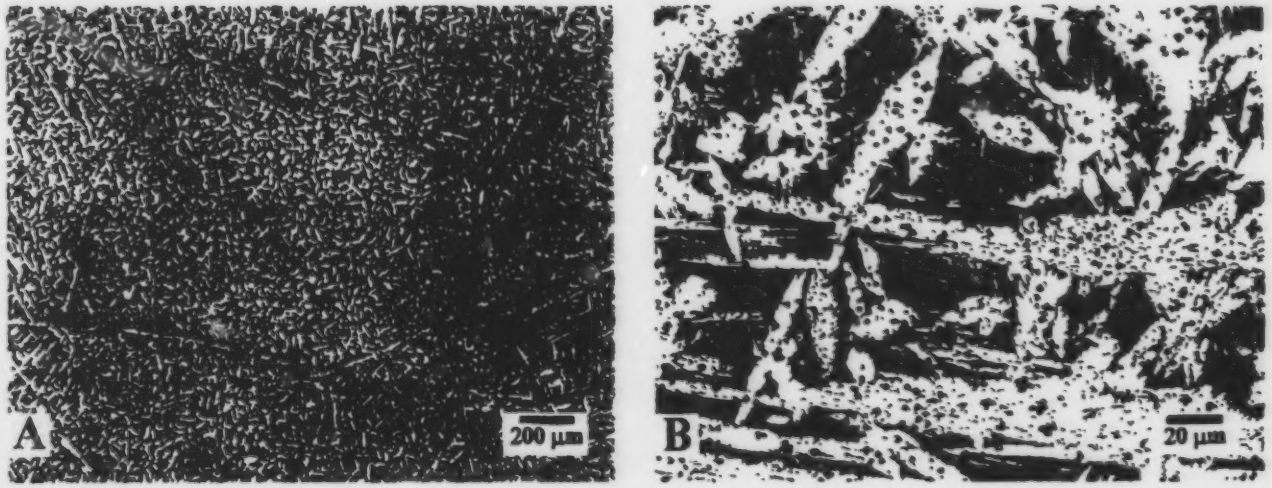

Fig. 22. Optical micrographs of sample 132-95-2 from alloy series B3 (11.3% Al, 4.1% Ni, 5.0% Fe). A coarsening of the α grains such that they are less acicular in nature is observed in (a). In (b) a high fraction of κ_{II} particles is observed, as well as some retained β phase.

CANMET

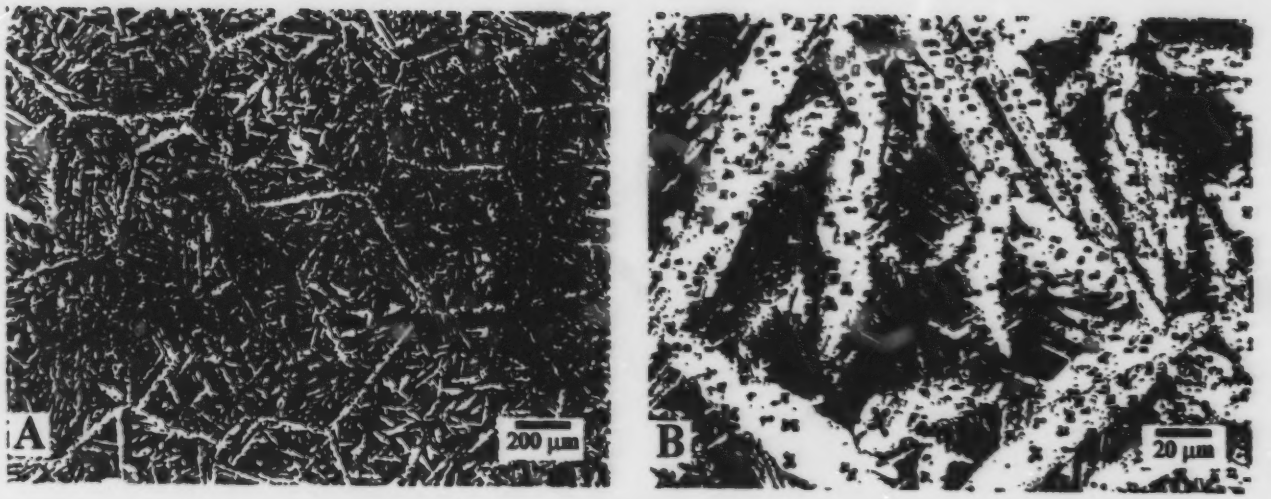

Fig. 23. Optical micrographs of sample 132-95-3 from alloy series B3 (11.3% Al, 4.0% Ni, 5.8% Fe). A decrease in the size of the prior β grains delineated by the prior β boundaries is observed in (a). A further coarsening of the α grains as well as of the κ_{II} particles is observed in (b).

CANMET

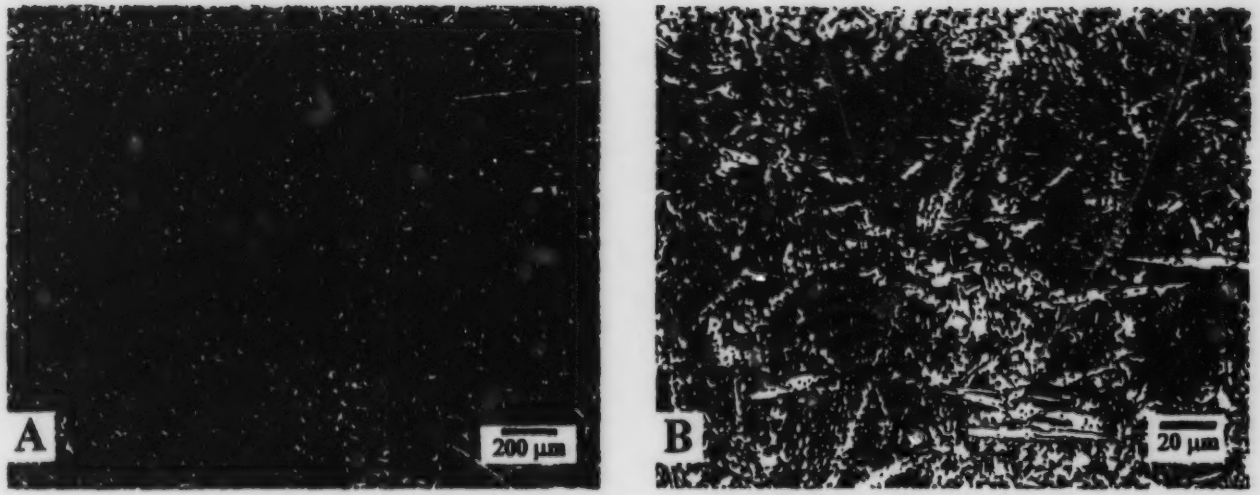

Fig. 24. Optical micrographs for sample 133-95-1 from alloy series B4 (12.2% Al, 4.7% Ni, 3.8% Fe). The prior β boundaries are clearly observed in (a), and a very fine lath-like structure of the α phase, similar to a bainitic or Widmanstatten structure is shown. A large number of κ_{II} particles are observed in (b).

CANMET

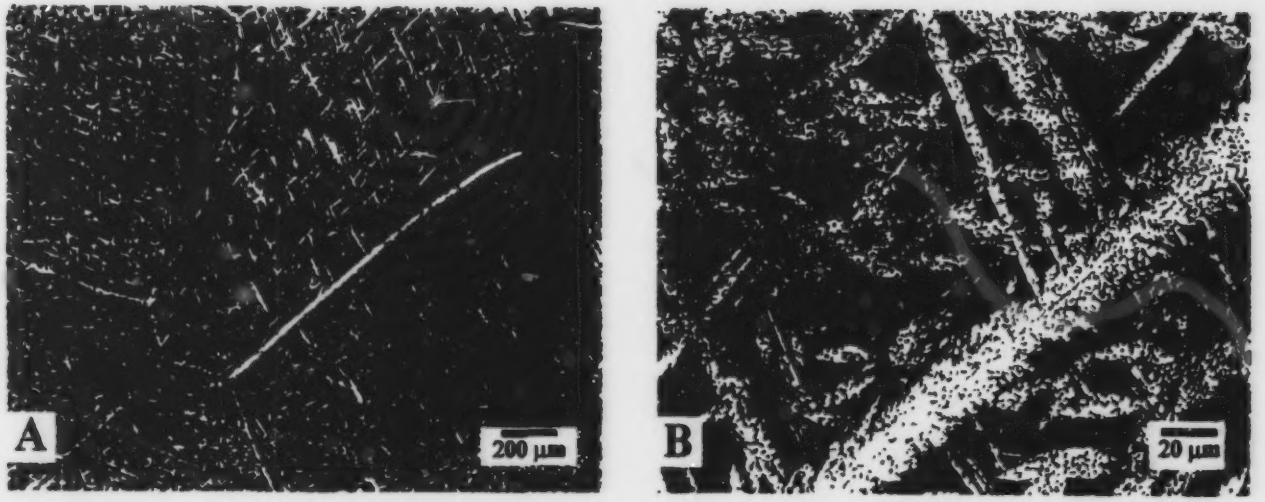

Fig. 25. Optical micrographs for sample 133-95-2 from alloy series B4 (12.2% Al, 5.9% Ni, 4.2% Fe). The prior β boundaries are again observed in (a), and a slight coarsening of the α grains has occurred. Again, a large number of κ_{II} particles are observed in (b).

CANMET

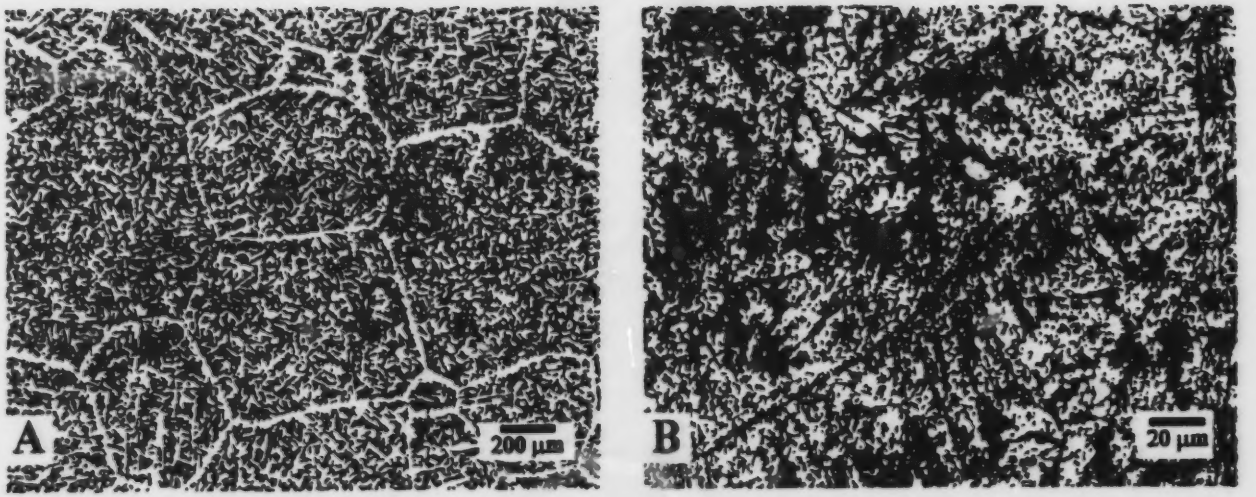

Fig. 26. Optical micrographs for sample 133-95-3 from alloy series B4 (12.2% Al, 6.1% Ni, 6.5% Fe). The prior β boundaries are again clear in (a), where a decrease in the size of the prior β grains is also evident. A coarsening of the α grains to a more columnar-like structure has also resulted. In (b), a coarsening of the κ_{II} phase is observed.

CANMET

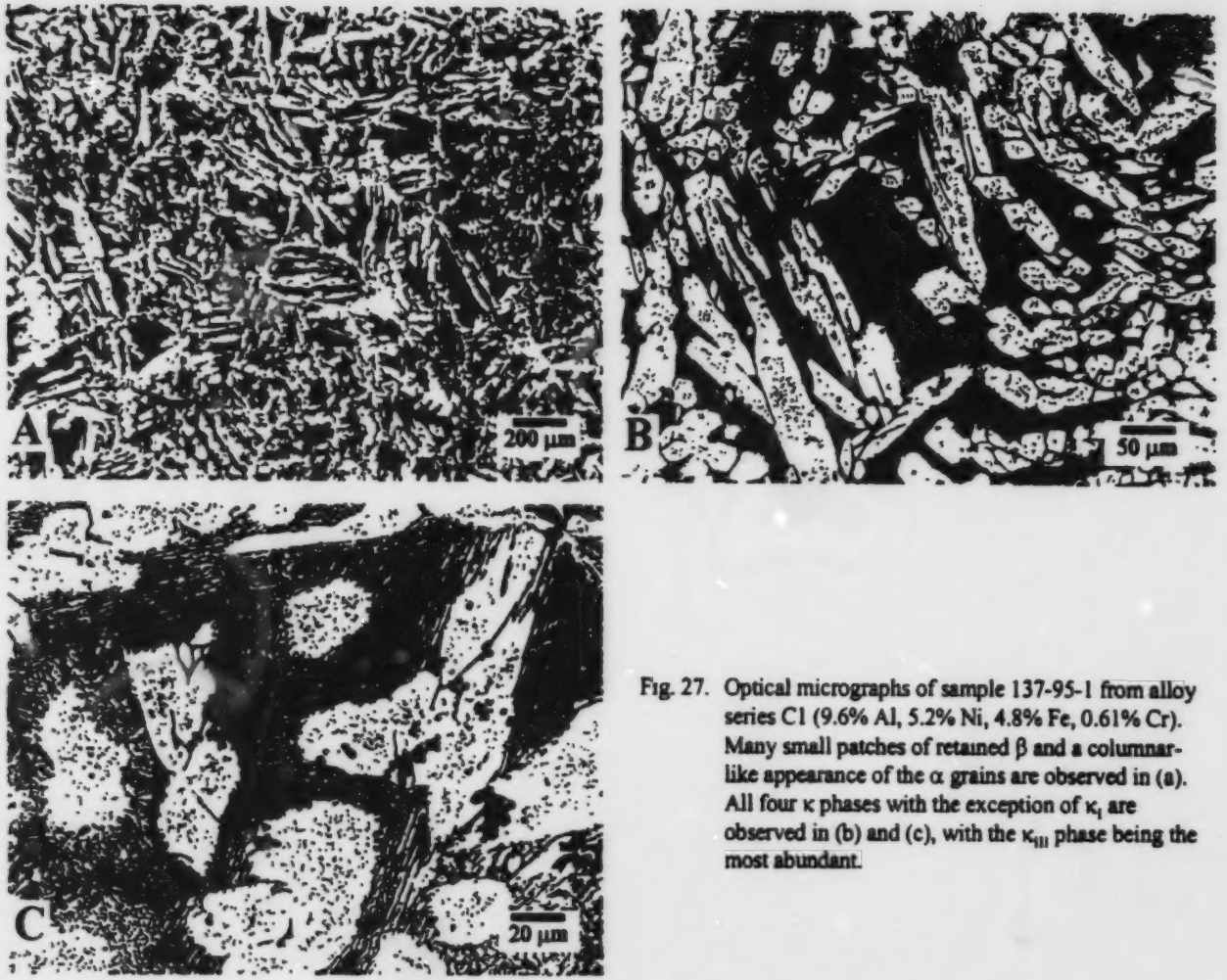

Fig. 27. Optical micrographs of sample 137-95-1 from alloy series C1 (9.6% Al, 5.2% Ni, 4.8% Fe, 0.61% Cr). Many small patches of retained β and a columnar-like appearance of the α grains are observed in (a). All four κ phases with the exception of κ_I are observed in (b) and (c), with the κ_{III} phase being the most abundant.

CANMET

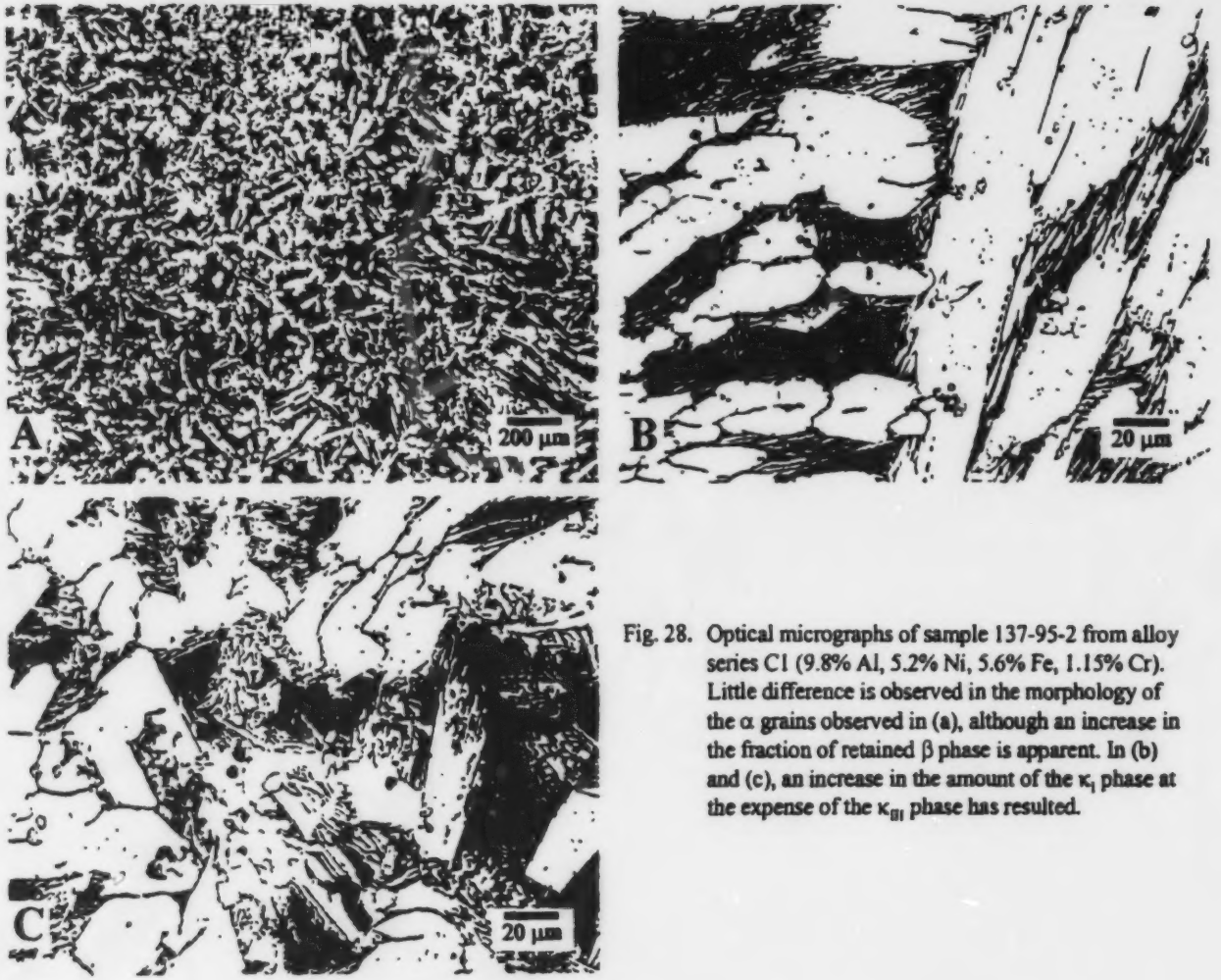

Fig. 28. Optical micrographs of sample 137-95-2 from alloy series C1 (9.8% Al, 5.2% Ni, 5.6% Fe, 1.15% Cr). Little difference is observed in the morphology of the α grains observed in (a), although an increase in the fraction of retained β phase is apparent. In (b) and (c), an increase in the amount of the κ_I phase at the expense of the κ_{III} phase has resulted.

CANMET

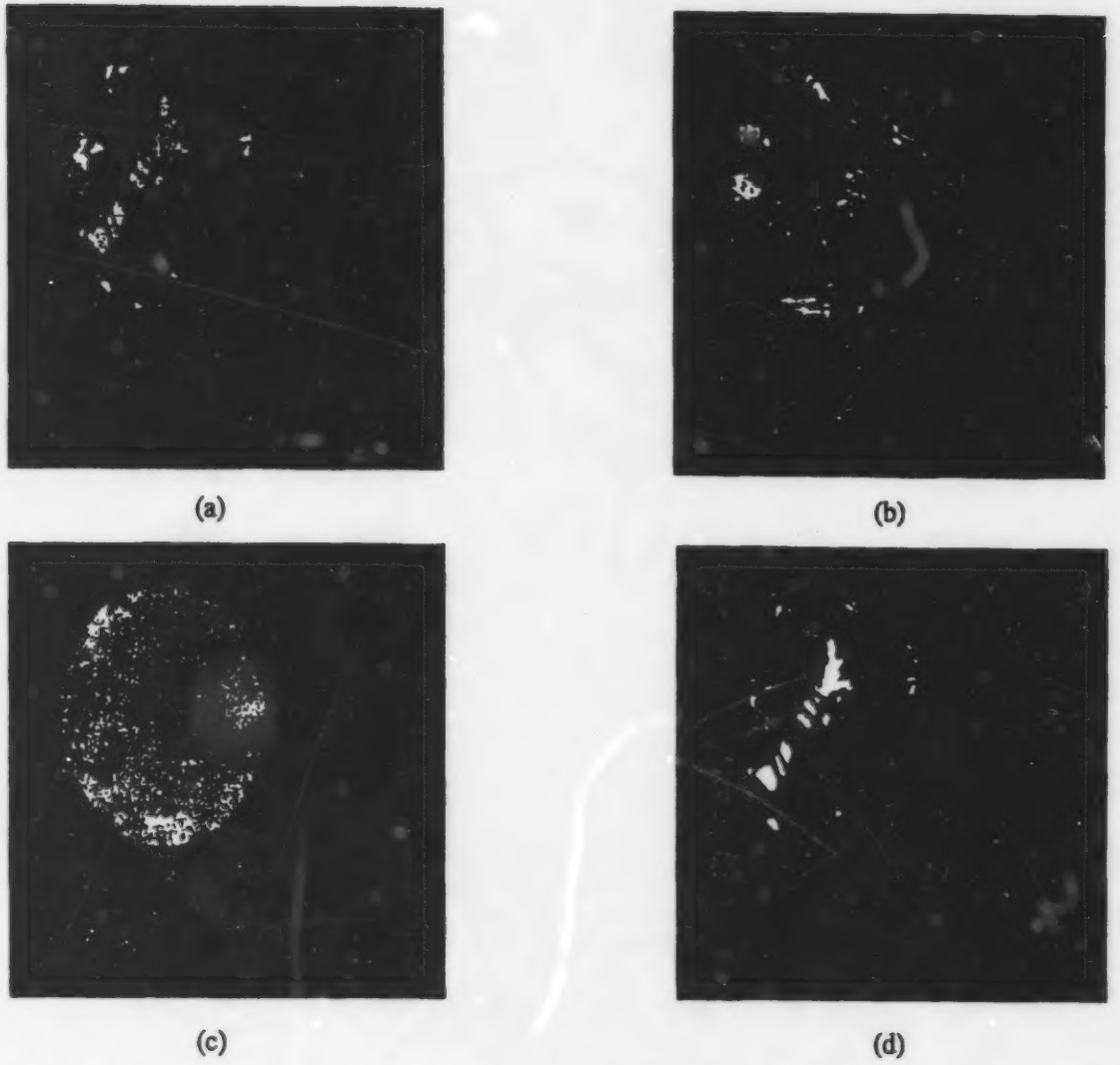

Fig. 29. SIMS direct ion images from sample 137-95-2 for (a) Fe, (b) Ni, (c) Cu and (d) Cr. The Fe and Cr enrichment of the κ_1 phase is striking. Enrichment in Ni of the κ_m phase is also evident. The field of view is 100 μm.

CANMET

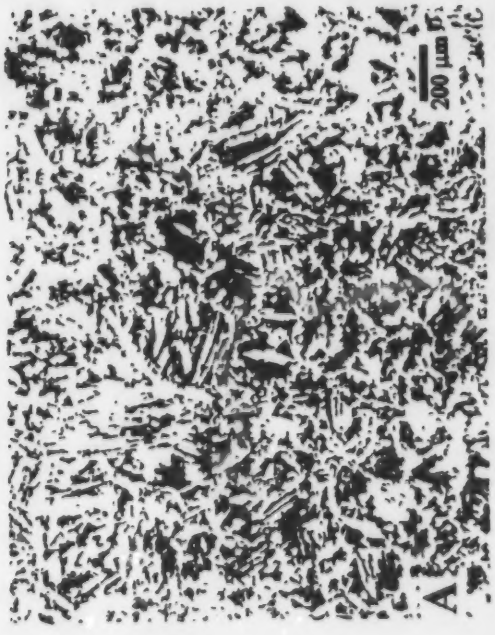

Fig. 30. Optical micrographs of sample 137-95-3 from alloy series C1 (9.6% Al, 5.1% Ni, 6.3% Fe, 1.72% Cr). A further increase in the amount of the retained β phase is observed in (a). In (b) and (c), the size and quantity of the κ_I is shown to increase dramatically. Extensive regions of κ_{III} are also visible.

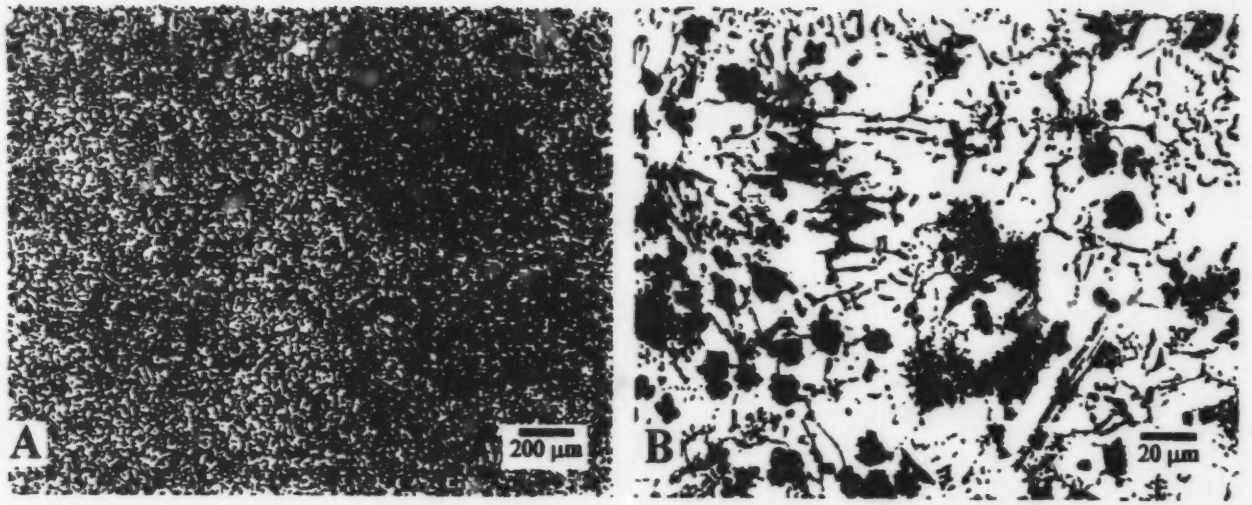

Fig. 31. Optical micrographs of sample 103-95-1 from alloy series C2 (10.0% Al, 5.0% Ni, 6.3% Fe, 1.08% Ti). The α grains show an equiaxed structure, with many small patches of retained β also visible. Numerous κ_I rosettes are shown in (b), along with κ_{II} and κ_{IV} phases.

CANMET

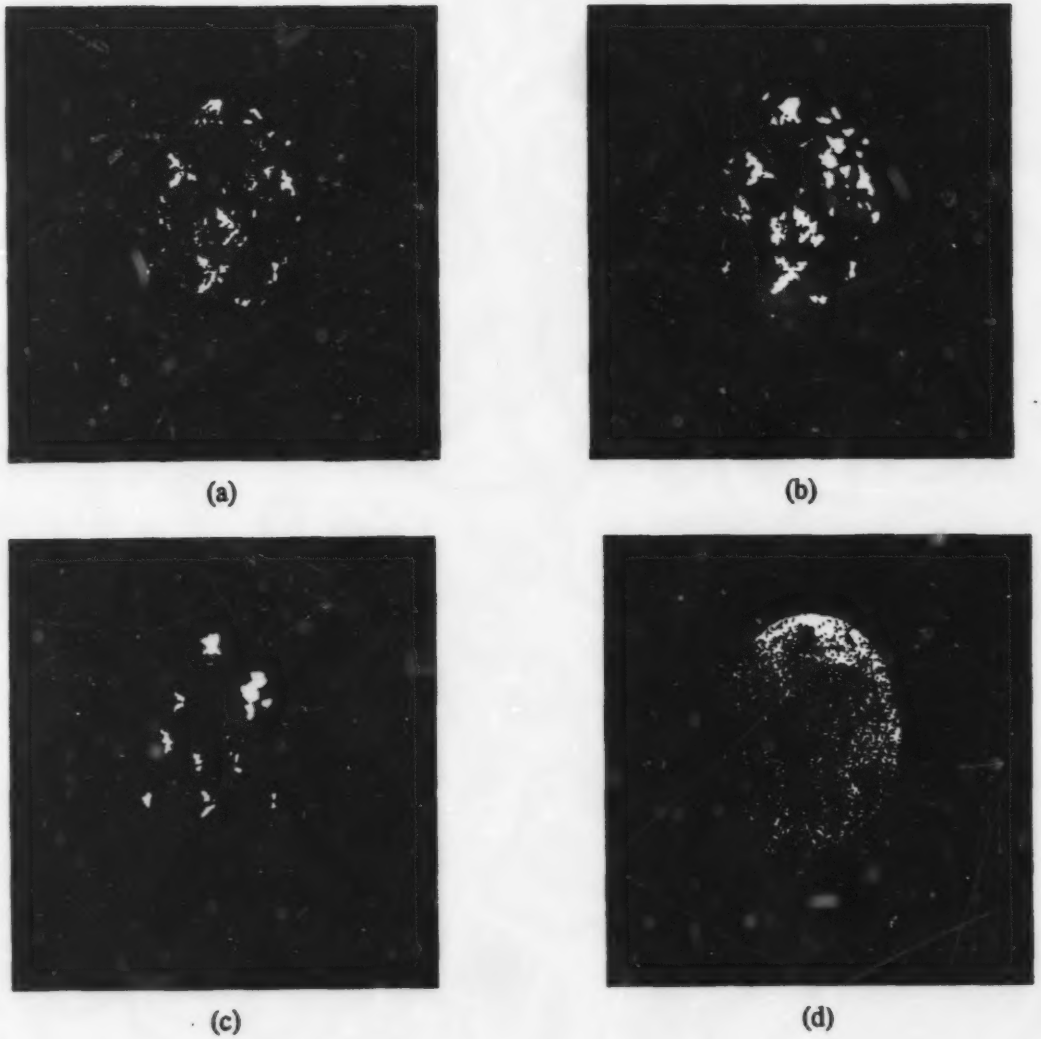

Fig. 32. SIMS direct ion images from sample 103-95-1 for (a) Fe, (b) Ni, (c) Ti and (d) Cu. The enrichment of the κ_1 rosettes in Fe, Ni and Ti is clear. The field of view is 100 μm.

CANMET

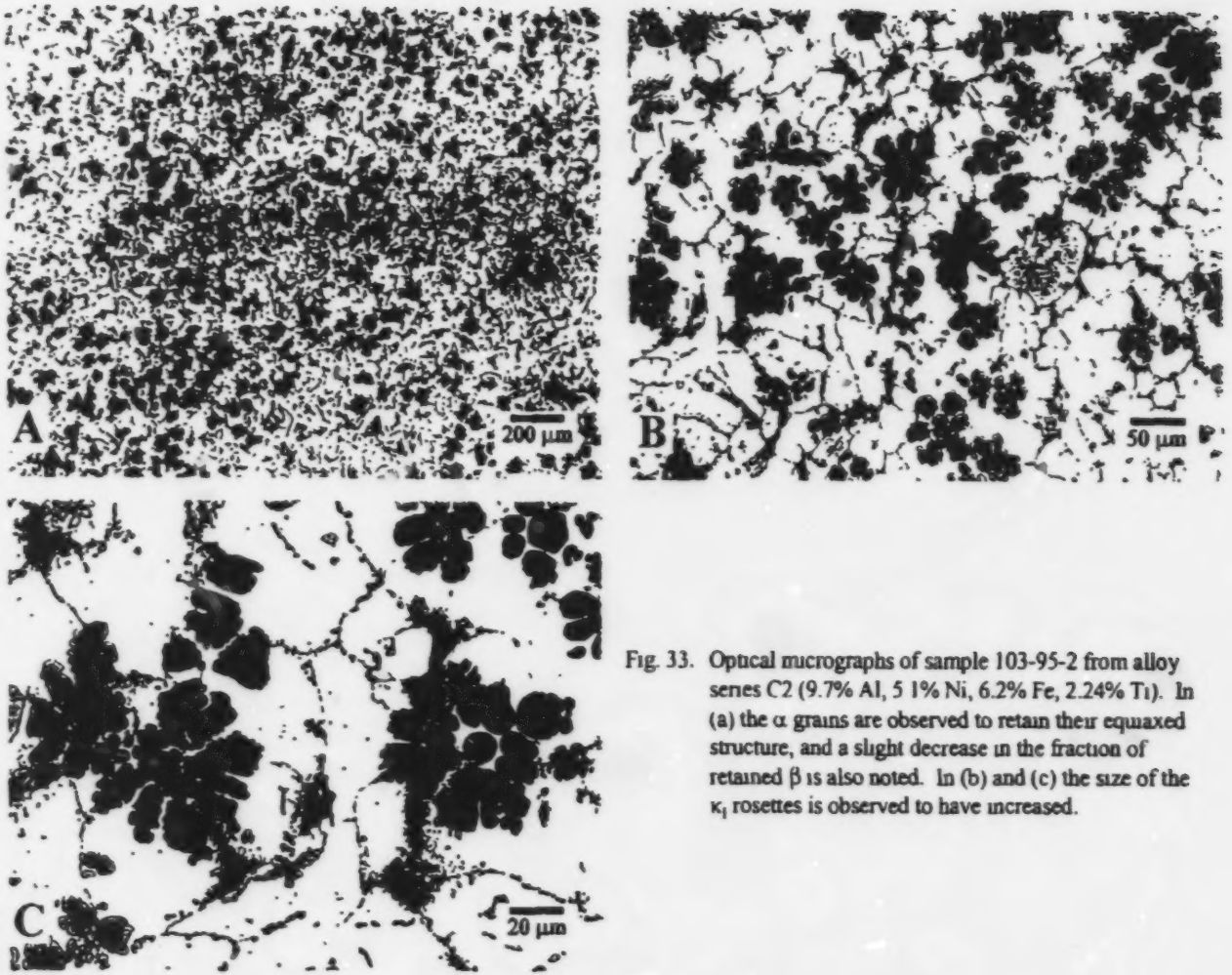

Fig. 33. Optical micrographs of sample 103-95-2 from alloy series C2 (9.7% Al, 5.1% Ni, 6.2% Fe, 2.24% Ti). In (a) the α grains are observed to retain their equiaxed structure, and a slight decrease in the fraction of retained β is also noted. In (b) and (c) the size of the κ_1 rosettes is observed to have increased.

CANMET

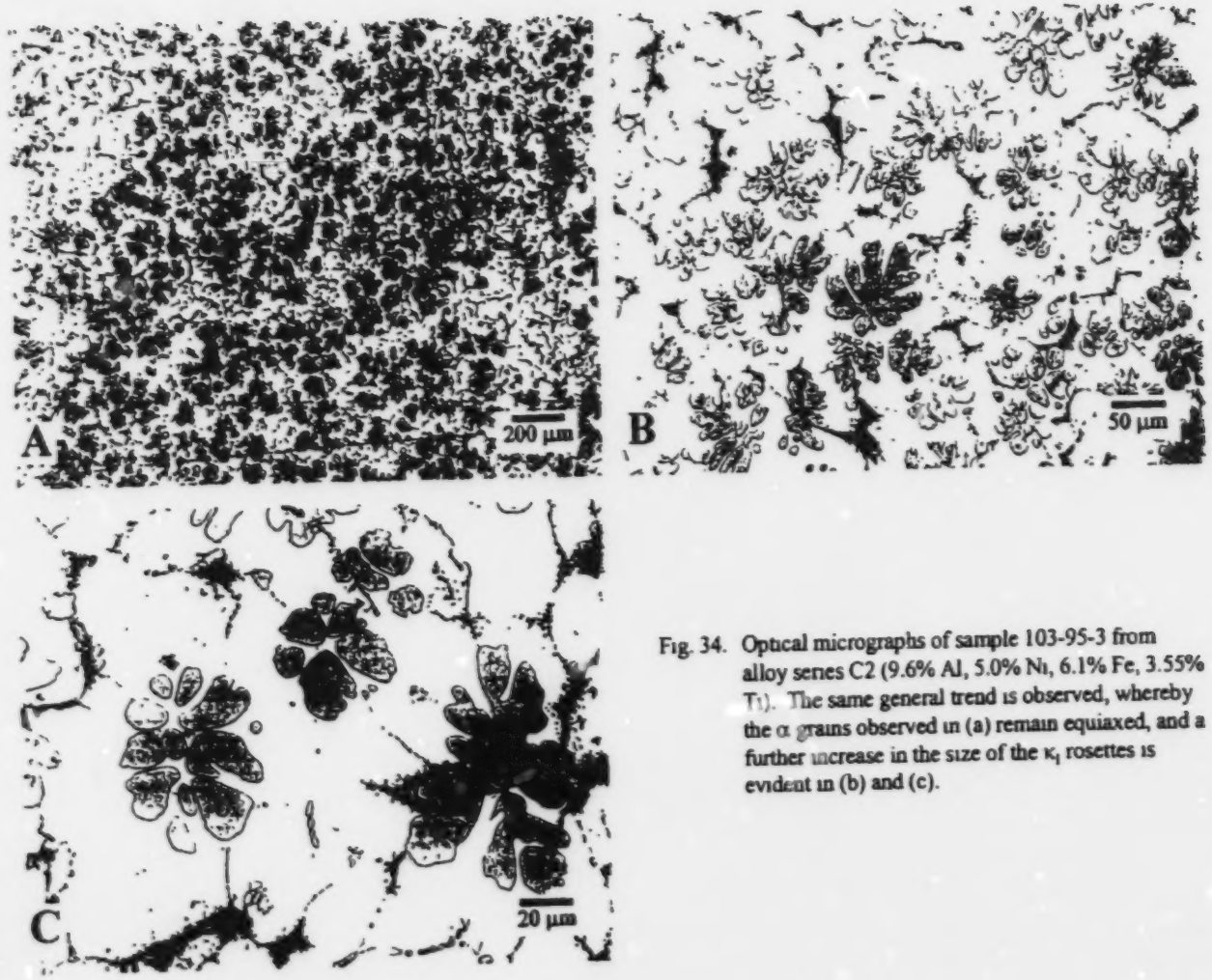

Fig. 34. Optical micrographs of sample 103-95-3 from alloy series C2 (9.6% Al, 5.0% Ni, 6.1% Fe, 3.55% Ti). The same general trend is observed, whereby the α grains observed in (a) remain equiaxed, and a further increase in the size of the κ_1 rosettes is evident in (b) and (c).

CANMET

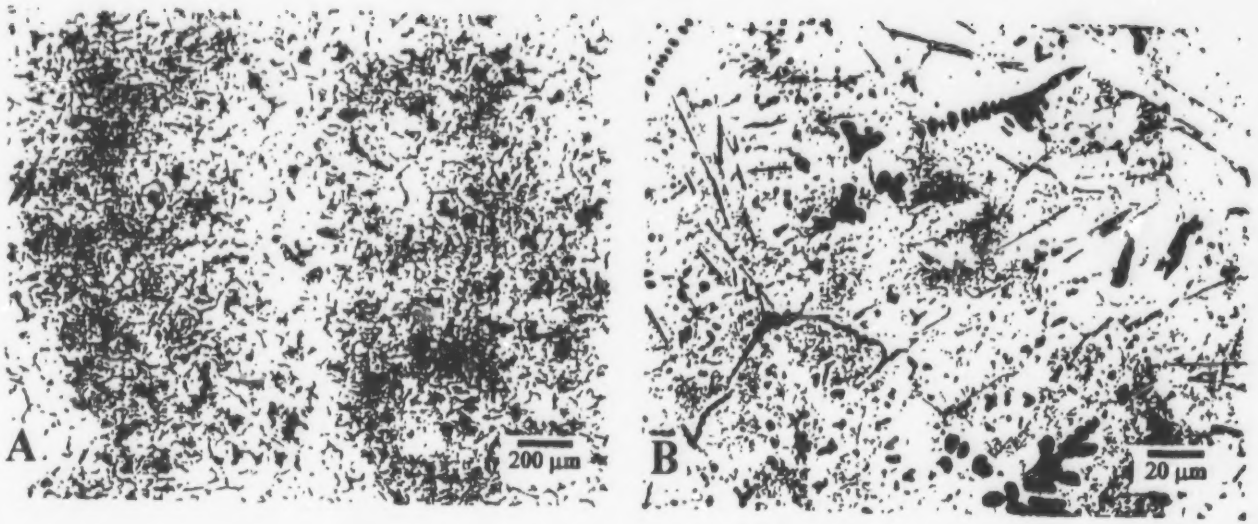

Fig. 35 Optical micrographs of sample 114-95-1 from alloy series C3 (9.4% Al, 5.0% Ni, 6.0% Fe, 0.97% Zr). Equiaxed α grains and small patches of retained β are observed in (a). At higher magnification the structure is characterized by the presence of all κ phases (although little κ_{III} is present) and by an unknown needle-like phase.

CANMET

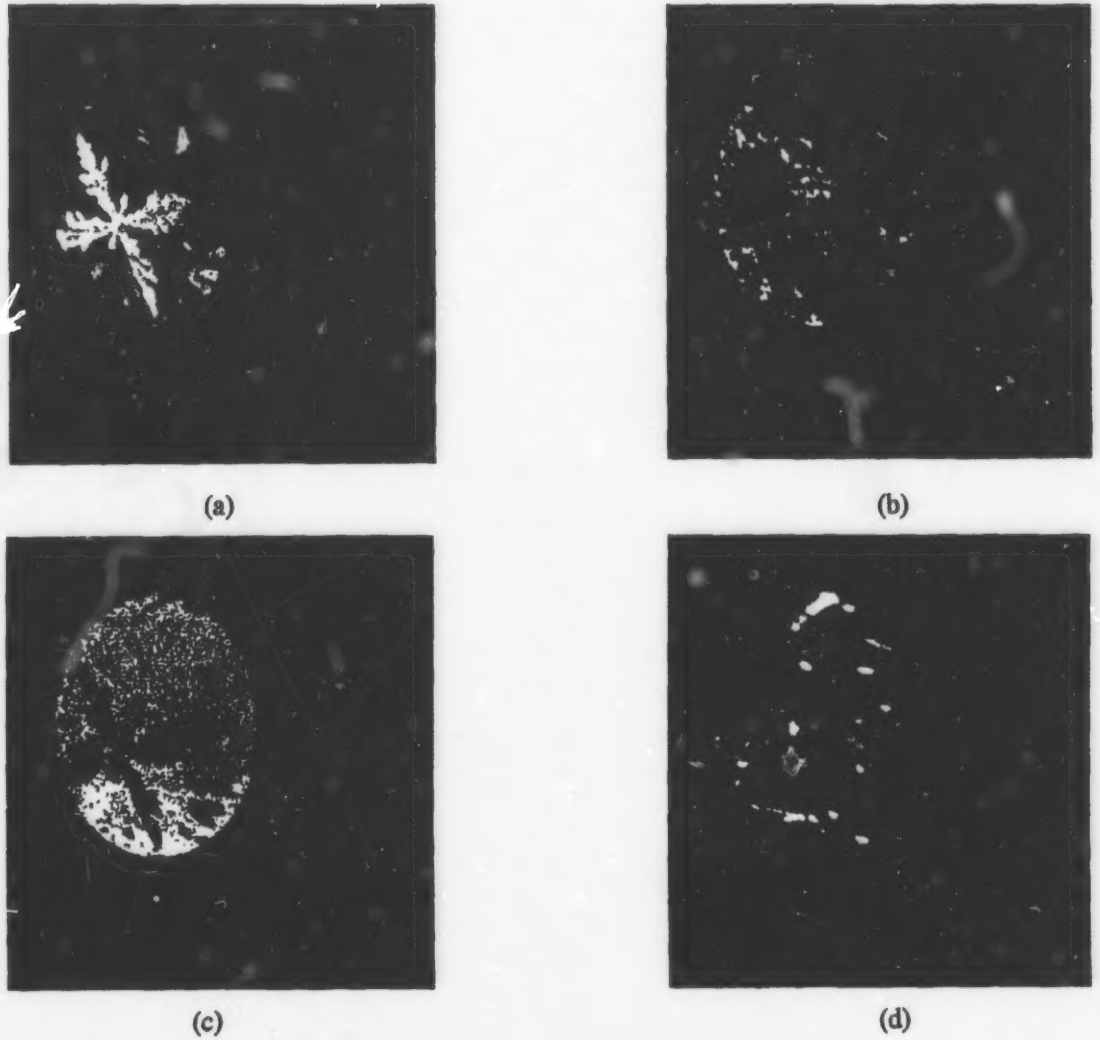

Fig. 36. SIMS direct ion images from sample 114-95-01 for (a) Fe, (b) Ni, (c) Cu and (d) Zr. An enrichment in Fe and variation of the Cu content in the κ_1 phase is evident. The needle-like phase is found to be enriched in Zr. The field of view is 100 μm.

CANMET

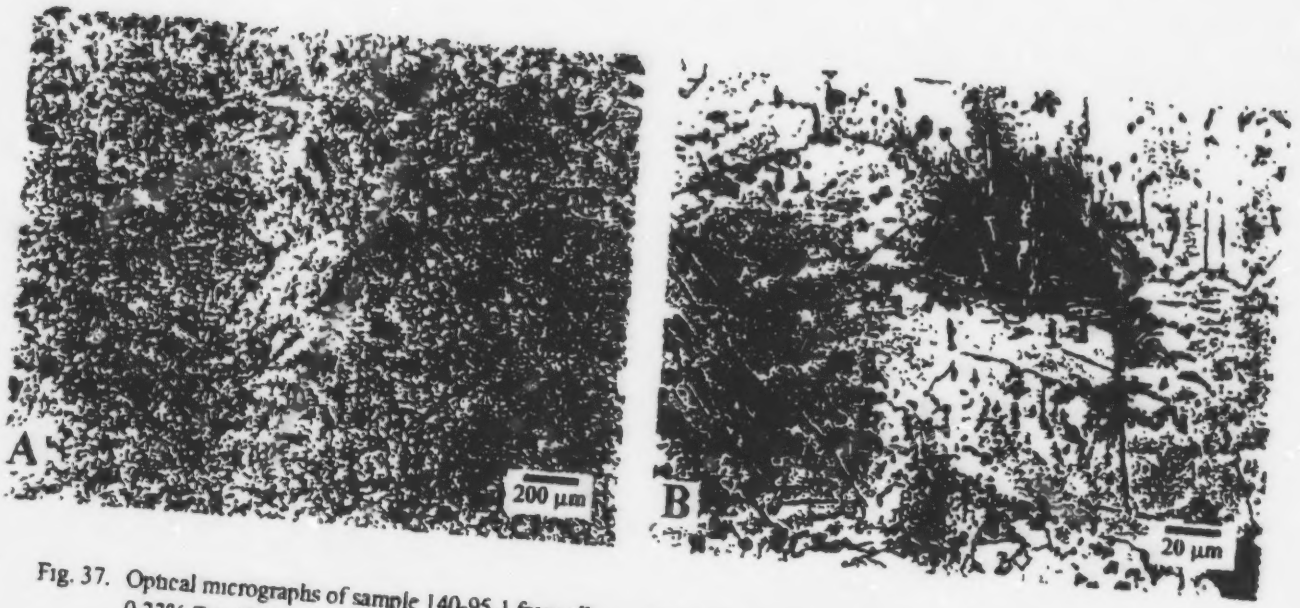

Fig. 37. Optical micrographs of sample 140-95-1 from alloy series D1 (9.3% Al, 4.9% Ni, 5.3% Fe, 0.31% Cr, 0.23% Ti, 0.23% Zr). Equiaxed α grains and a significant fraction of retained β phase are observed in (a). All κ phases are observed in (b), as well as the unknown needle-like phase

CANMET

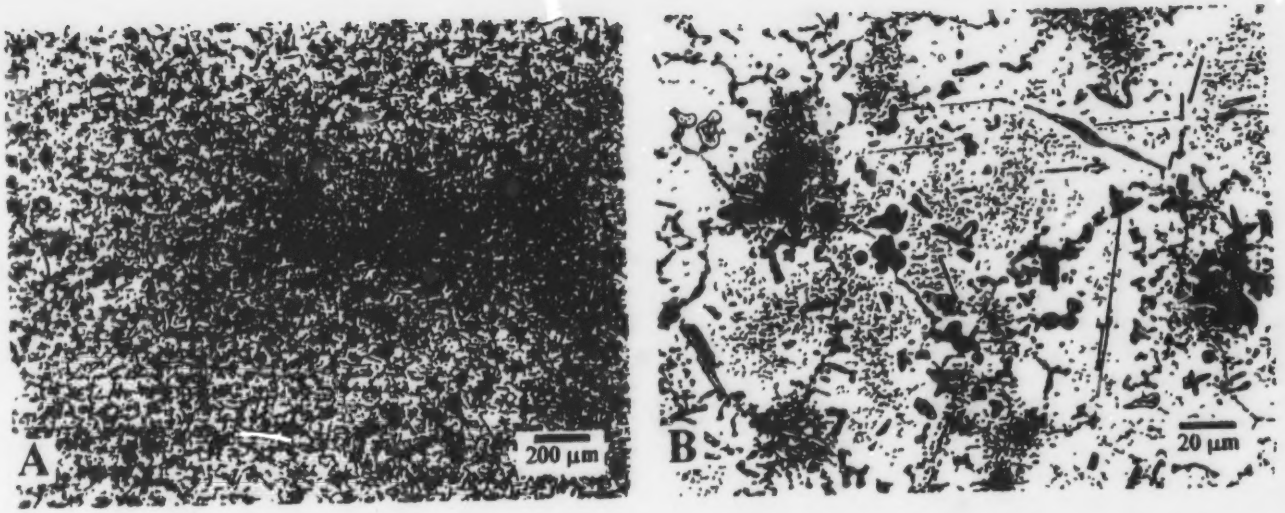

Fig 38 Optical micrographs of sample 140-95-2 from alloy series D1 (8.9% Al, 4.7% Ni, 5.0% Fe, 0.60% Cr, 0.44% Ti, 0.41% Zr) The α grains remain equiaxed in nature and a significant fraction of retained β is also visible In (b) all κ phases as well as the needle-like phase are observed

CANMET

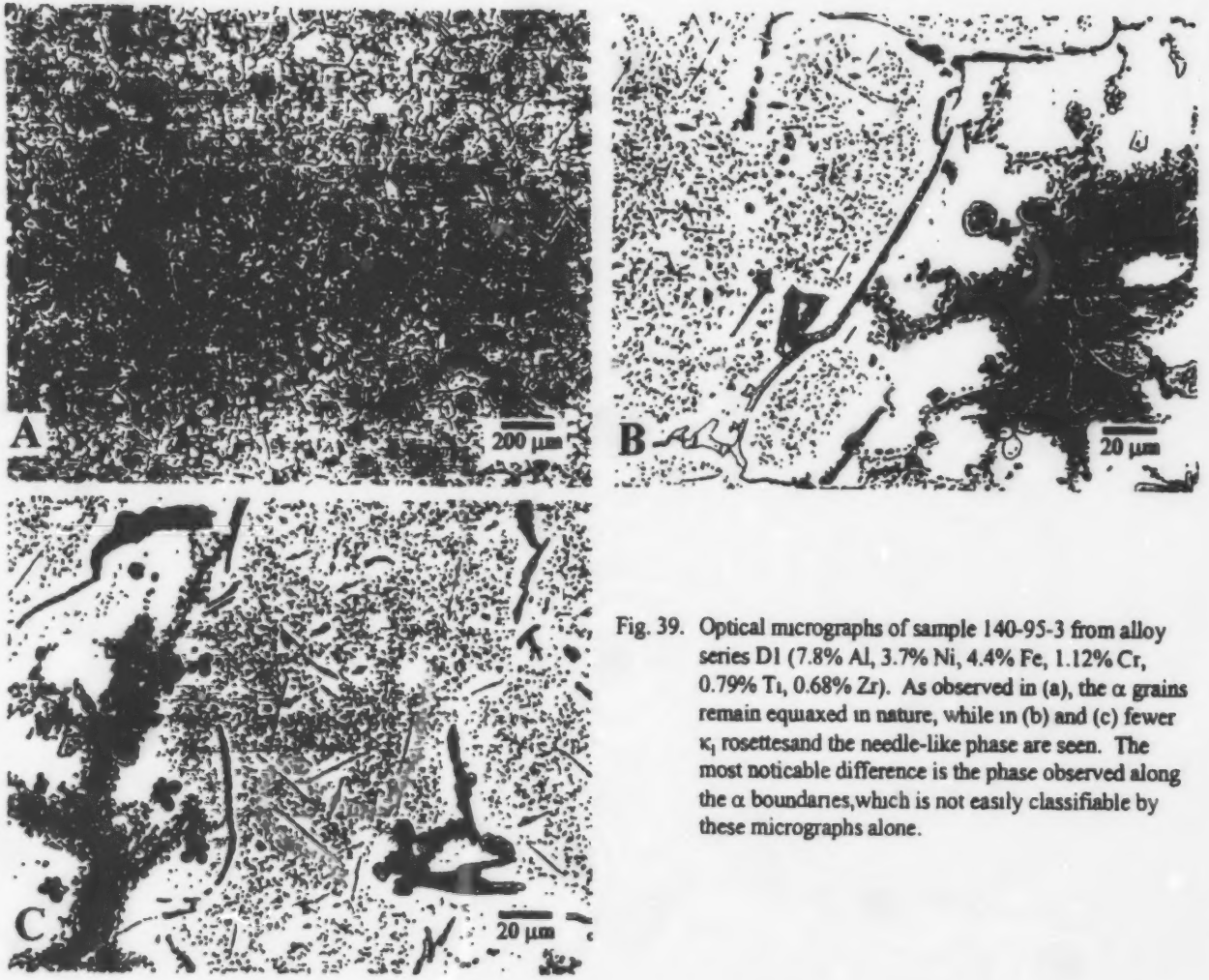

Fig. 39. Optical micrographs of sample 140-95-3 from alloy series D1 (7.8% Al, 3.7% Ni, 4.4% Fe, 1.12% Cr, 0.79% Ti, 0.68% Zr). As observed in (a), the α grains remain equiaxed in nature, while in (b) and (c) fewer κ_1 rosettesand the needle-like phase are seen. The most noticable difference is the phase observed along the α boundaries,which is not easily classifiable by these micrographs alone.

CANMET

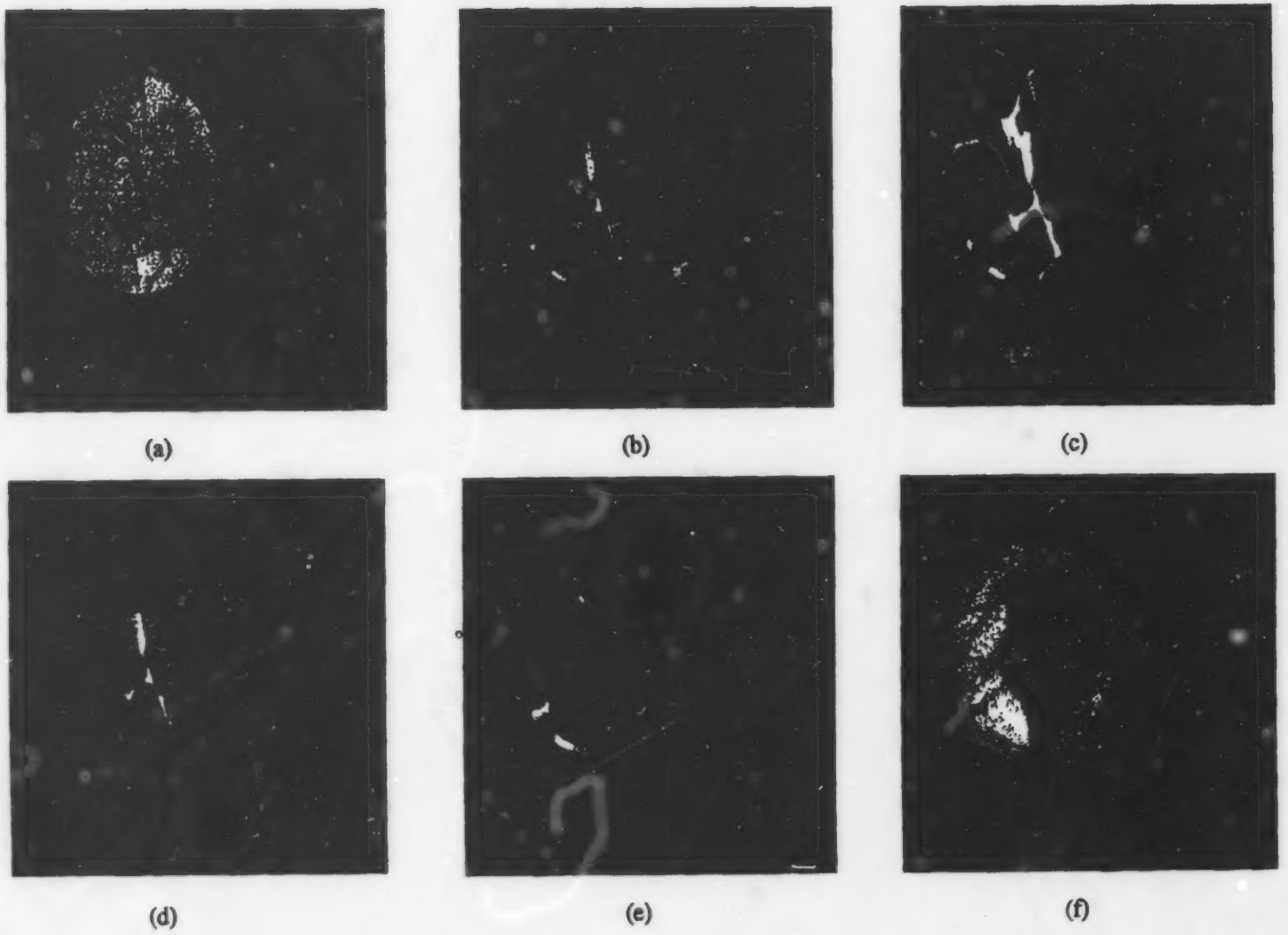

Fig. 40. SIMS direct ion images from sample 140-95-3 for (a) Al, (b) Ti, (c) Fe, (d) Cr, (e) Ni and (f) Cu. The boundary phase appears to be enriched in Ti, Cr, Zr and Fe, while showing a depletion of Ni, Cu and Al. The field of view is 100 μm.

CANMET

(g)

Fig. 40 (cont'd). SIMS direct ion image from sample 140-95-3 for (g) Zr. The boundary phase appears to be enriched in Ti, Cr, Zr and Fe, while showing a depletion of Ni, Cu and Al. The field of view is 100 μm.

CANMET

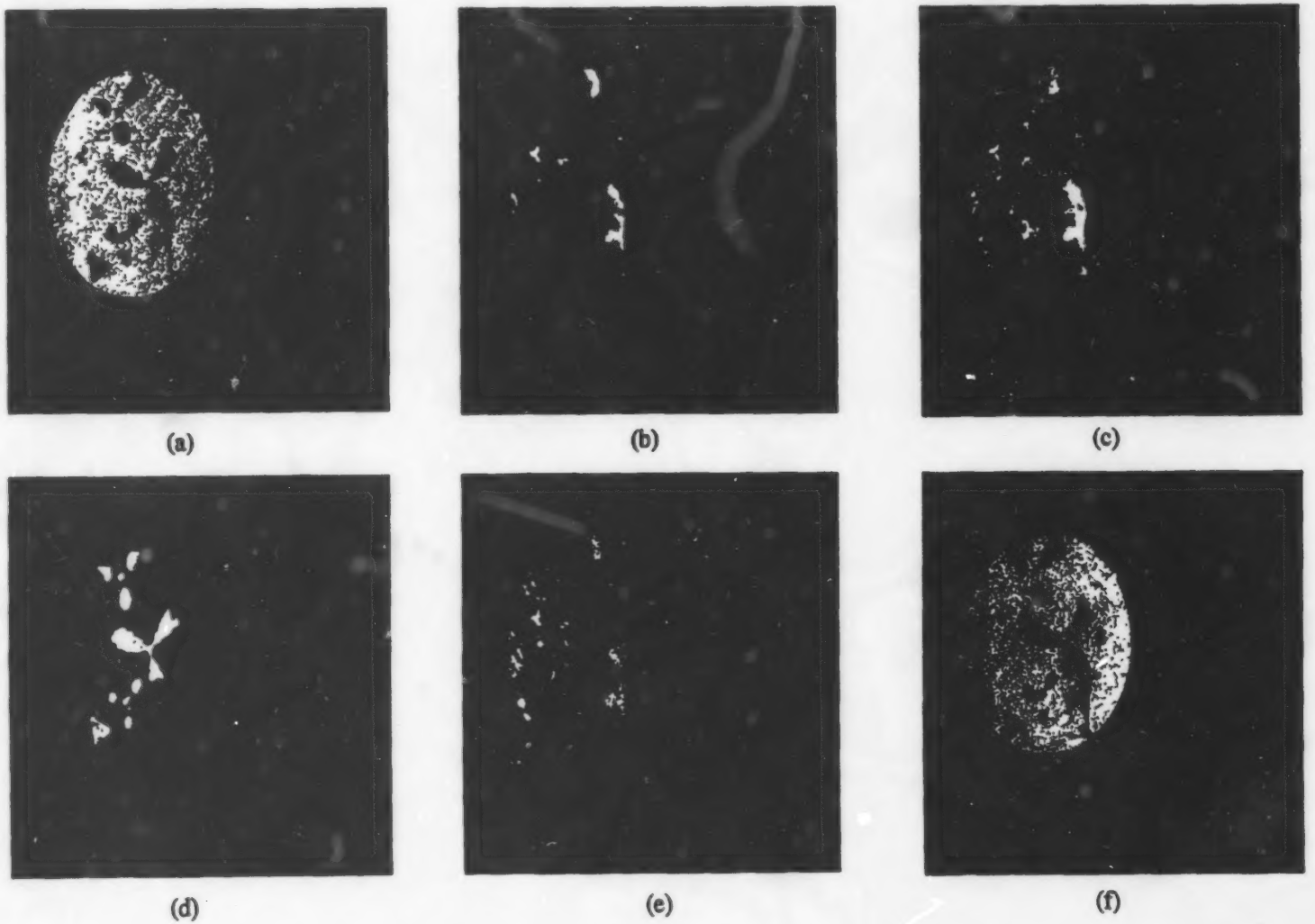

Fig. 41. SIMS direct ion images from sample 140-95-3 for (a) Al, (b) Ti, (c) Fe, (d) Cr, (e) Ni and (f) C. The κ_I rosettes are found to be enriched in Fe, Cr and to a lesser extent Ni, Ti and Zr. A depletion of Cu is also observed. The smaller κ_{II} particles show enrichments in Fe, Ti and Ni, with weaker enrichments in Cr and Zr. The field of view is 100 μm.

CANMET

(g)

Fig. 41 (cont'd). SIMS direct ion images from sample 140-95-3 for (g) Zr. The κ_I rosettes are found to be enriched in Fe, Cr and to a lesser extent Ni, Ti and Zr. A depletion of Cu is also observed. The smaller κ_{II} particles show enrichments in Fe, Ti and Ni, with weaker enrichments in Cr and Zr. The field of view is 100 μm.

CANMET

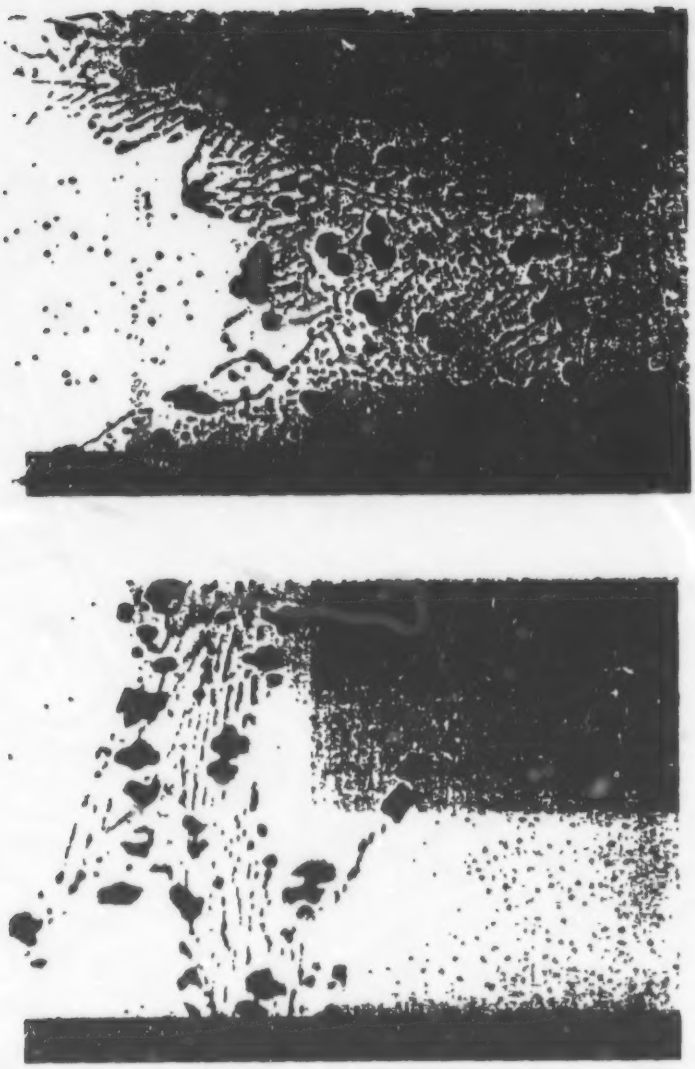

Fig. 42. SEM backscatter micrographs of sample 124-95-1 indicating areas analyzed by EDX. The results of the analyses are given in Table 15. .

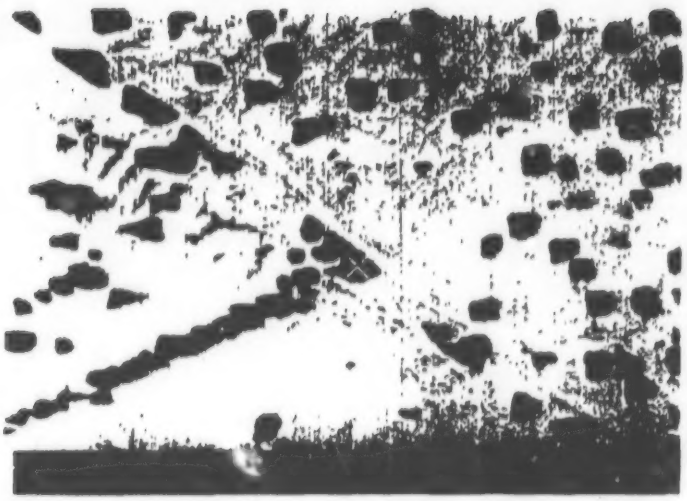

Fig. 43. SEM backscatter micrograph from sample 124-95-3 indicating areas analyzed with EDX. The results are summarized in Table 16.

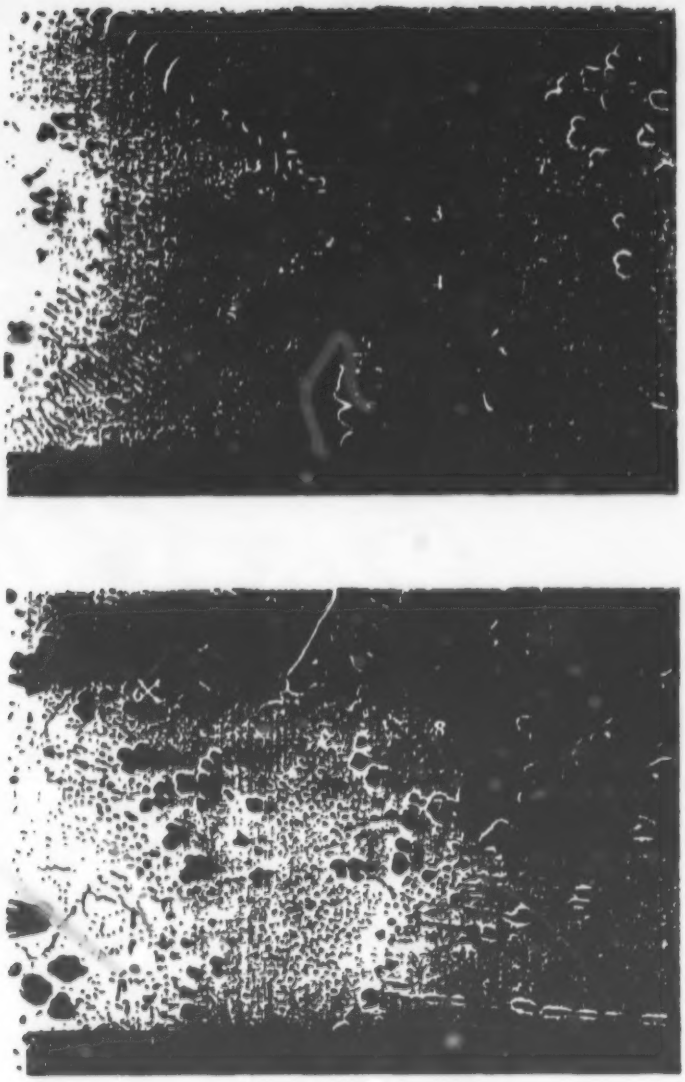

Fig. 44 SEM backscatter micrographs from sample 136-95-2 showing areas analyzed by EDX. The results are tabulated in Table 17.

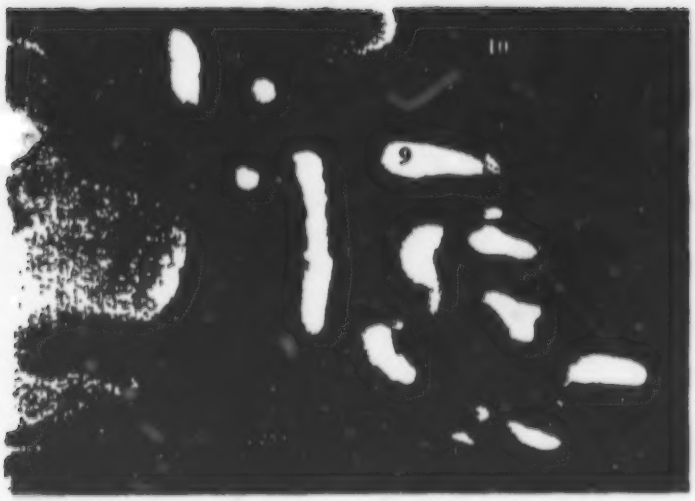

Fig. 44 (cont'd). SEM backscatter micrographs from sample 136-95-2 showing areas analyzed by EDX. The results are tabulated in Table 17.

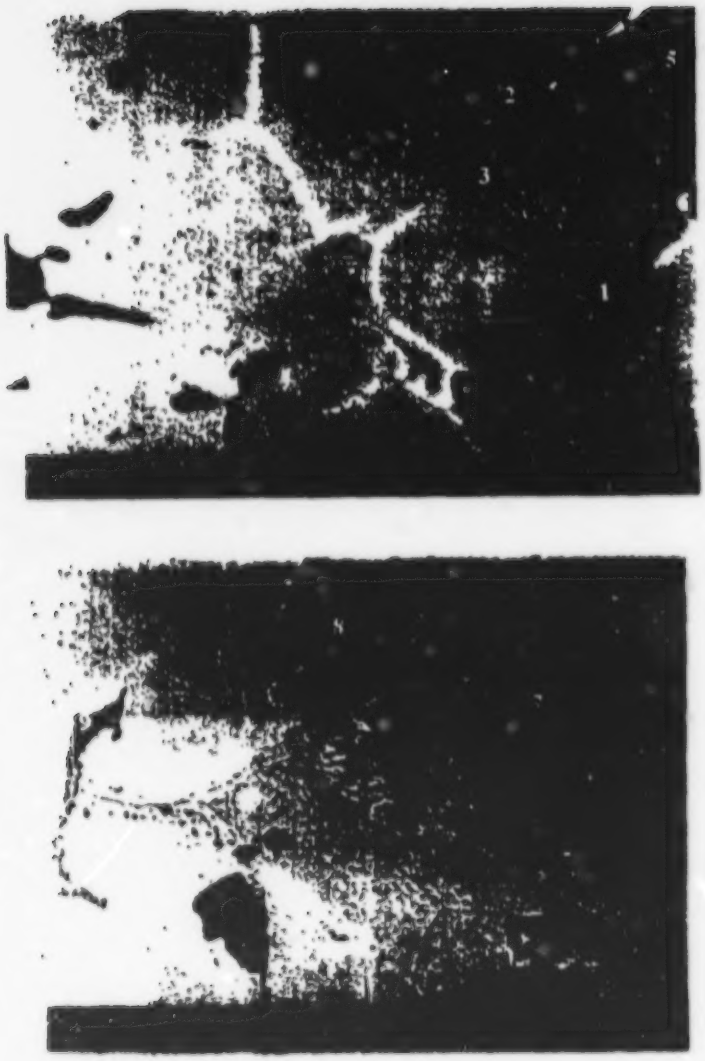

Fig. 45 SEM backscatter micrographs from sample 140-95-3 showing areas analyzed by EDX. The results are tabulated in Table 18.

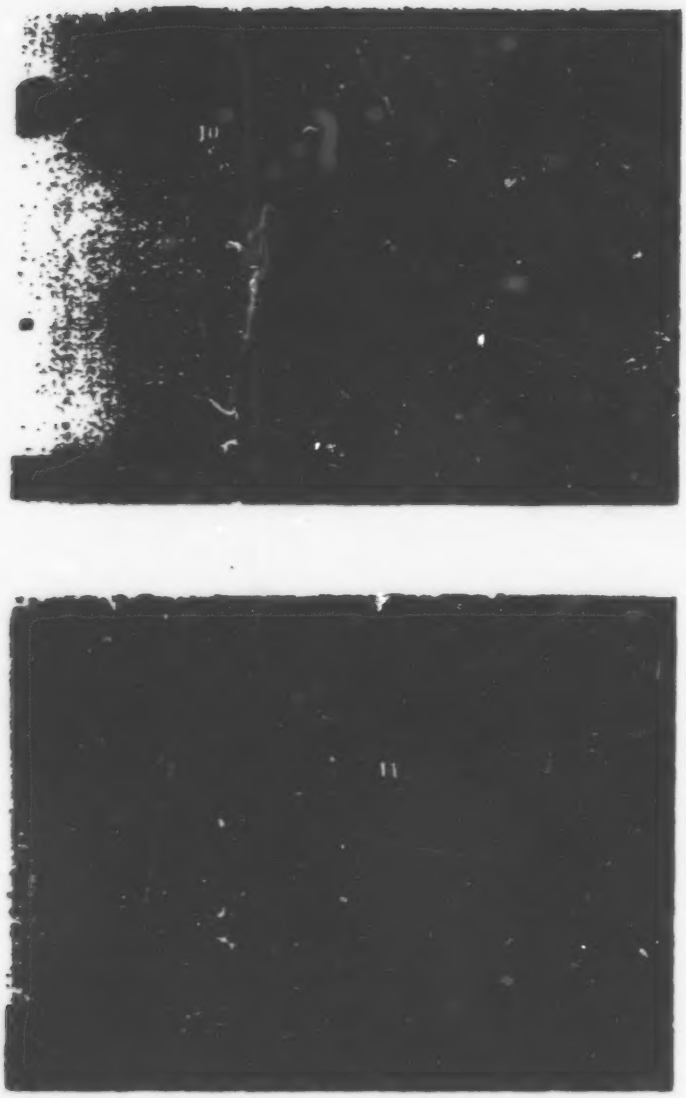

Fig. 45 (cont'd). SEM backscatter micrographs from sample 140-95-3 showing areas analyzed by EDX. The results are tabulated in Table 18.

UNCLASSIFIED
SECURITY CLASSIFICATION OF FORM
(highest classification of Title, Abstract, Keywords)

DOCUMENT CONTROL DATA

(Security classification of title, body of abstract and indexing annotation must be entered when the overall document is classified)

1 ORIGINATOR (the name and address of the organization preparing the document Organizations for whom the document was prepared, e g Establishment sponsoring a contractor's report, or tasking agency, are entered in section 8)

Materials Technology Laboratory (CANMET)
568 Booth St Ottawa, ON K1A 0G1

2 SECURITY CLASSIFICATION (overall security classification of the document including special warning terms if applicable)

Unclassified

3 TITLE (the complete document title as indicated on the title page Its classification should be indicated by the appropriate abbreviation (S,C,R or U) in parentheses after the title)

Microstructural Characterization of Sand Cast Ni-Al Bronzes (U)

4 AUTHORS (Last name first name, middle initial If military, show rank, e g Doe, Maj John E)

G. McMahon, J.A. Gianetto and M. Sahoo

5 DATE OF PUBLICATION (month and year of publication of document)

April 1999

6a NO OF PAGES (total containing information Include Annexes, Appendices, etc)

75 (approx.)

6b. NO. OF REFS (total cited in document)

9

7 DESCRIPTIVE NOTES (the category of the document, e g technical report, technical note or memorandum If appropriate, enter the type of report, e g interim, progress summary, annual or final Give the inclusive dates when a specific reporting period is covered)

Contractor Report

8 SPONSORING ACTIVITY (the name of the department project office or laboratory sponsoring the research and development Include address)

Defence Research Establishment Atlantic

9a PROJECT OR GRANT NO (if appropriate, the applicable research and development project or grant number under which the document was written Please specify whether project or grant)

Project 1gh-16

9b. CONTRACT NO (if appropriate, the applicable number under which the document was written)

10a ORIGINATOR'S DOCUMENT NUMBER (the official document number by which the document is identified by the originating activity This number must be unique to this document)

MTL 97-02(TR-R)

10b OTHER DOCUMENT NOs (Any other numbers which may be assigned this document either by the originator or by the sponsor)

DREA CR 1999 -042

11 DOCUMENT AVAILABILITY (any limitations on further dissemination of the document, other than those imposed by security classification)

(X) Unlimited distribution
( ) Defence departments and defence contractors; further distribution only as approved
( ) Defence departments and Canadian defence contractors; further distribution only as approved
( ) Government departments and agencies; further distribution only as approved
( ) Defence departments; further distribution only as approved
( ) Other (please specify):

12 DOCUMENT ANNOUNCEMENT (any limitation to the bibliographic announcement of this document This will normally correspond to the Document Availability (11) However, where further distribution (beyond the audience specified in (11) is possible, a wider announcement audience may be selected)

Unlimited

UNCLASSIFIED
SECURITY CLASSIFICATION OF FORM

UNCLASSIFIED
SECURITY CLASSIFICATION OF FORM
(highest classification of Title, Abstract, Keywords)

13 ABSTRACT (a brief and factual summary of the document. It may also appear elsewhere in the body of the document itself. It is highly desirable that the abstract of classified documents be unclassified. Each paragraph of the abstract shall begin with an indication of the security classification of the information in the paragraph (unless the document itself is unclassified) represented as (S), (C), (R), or (U). It is not necessary to include here abstracts in both official languages unless the text is bilingual)

A study of the effect of alloy chemistry on the microstructure and microhardness of nickel aluminum bronze (NAB) with systematic changes in the Ni, Fe and Al content has been carried out for the reference alloy C95800. A further set of castings was made in order to investigate the effect of Cr, Ti and Zr additions, both singly and in combination, on the resultant microstructure and microhardness. All castings were characterized using optical microscopy and microhardness testing, and a select group was further characterized using scanning electron microscopy (SEM) and energy dispersive X-ray analysis (EDX). Most of these samples were also examined by secondary ion mass spectrometry (SIMS). The microstructures were found to be very sensitive to small changes in alloy chemistry.

14. KEYWORDS, DESCRIPTORS or IDENTIFIERS (technically meaningful terms or short phrases that characterize a document and could be helpful in cataloguing the document. They should be selected so that no security classification is required. Identifiers, such as equipment model designation, trade name, military project code name, geographic location may also be included. If possible keywords should be selected from a published thesaurus, e.g. Thesaurus of Engineering and Scientific Terms (TEST) and that thesaurus-identified. If it not possible to select indexing terms which are Unclassified, the classification of each should be indicated as with the title)

Nickel Aluminum Bronze
Casting
Microstructure
Auger
SIMS

UNCLASSIFIED
SECURITY CLASSIFICATION OF FORM